Journal of Materials Chemistry A

ROYAL SOCIETY OF CHEMISTRY

REVIEW

View Article Online
View Journal | View Issue

Cite this: *J. Mater. Chem. A*, 2021, **9**, 1429

Structurally and chemically engineered graphene for capacitive deionization

Liang Chang,† Yuhuan Fei† and Yun Hang Hu *

Highly efficient capacitive deionization (CDI) relies on unimpeded transport of salt ions to the electrode surface. Graphene is an ideal candidate to provide superb conditions for ion adsorption as it possesses high theoretical surface area and electrical conductivity. When ions are stored solely within the electric double layers (EDLs), a hydrophilic graphene surface with hierarchical pores can maximize the accessible surface area and promote the ion transport. In the case of synergistic ion storage *via* electrostatic adsorption and faradaic redox reaction, graphene can act as both the electron highway and the reciprocal spacer to provide surface-confined effects. Substantially, structural and chemical engineering towards graphene can enhance the ion removal capacity and rate, and improve the charge efficiency and ion selectivity. In this review, we keep pace with the in-depth studies of CDI technologies and recent progress on graphene-based materials for CDI. Major challenges in the rational assembly of the desired material functionalities in terms of surface area, pore structure, and hydrophilicity are addressed. As electrode materials develop, the ultimate goal is to achieve highly efficient, energy-saving, and environment-friendly CDI.

Received 15th October 2020
Accepted 4th December 2020

DOI: 10.1039/d0ta10087k

rsc.li/materials-a

1. Introduction

Desalination is a popular technology to handle the global freshwater crisis since it exploits saline water, which makes up 97% of the earth's water resource, as the freshwater source.[1,2] The thermal, pressure, and electrical driving forces can be used to facilitate water–salt separation, resulting in the development of various technologies (*e.g.*, reverse osmosis (RO), multi-stage flash, multi-effect distillation, and electrodialysis).[3–5] The most attention has been paid to capacitive deionization (CDI), which separates salts from saline water through ion adsorption on a pair of polarized electrodes with a driving force lower than 2 V under ambient pressure.[6–9] Though the current CDI technology is inferior in energy consumption and efficiency compared to the most mature RO process,[3,10,11] the CDI possesses a great potential to become an energy-efficient, cost-effective, and environmentally friendly desalination process by developing efficient electrode materials,[12,13] prolonging the lifespan of

Department of Materials Science and Engineering, Michigan Technological University, Houghton, MI 49931-1295, USA. E-mail: yunhangh@mtu.edu; Tel: +1 9064872261

† The authors contributed equally to this manuscript.

Liang Chang received bachelor's and master's degrees from Wuhan University of Technology (China) in 2010 and 2012, respectively. She became a Ph.D. graduate student in Prof. Yun Hang Hu's group at Michigan Technological University (USA) in 2013 and obtained a Ph.D. degree in 2018. Then, as a post-doctoral fellow, she joined Prof. Allen Bard's group at University of Texas at Austin. Her research focuses on advanced materials for electrochemical applications, such as supercapacitors, capacitive deionization, batteries, and electrocatalysis.

Yuhuan Fei is currently pursuing her PhD under the supervision of Prof. Hu at the Department of Materials Science and Engineering, Michigan Technological University (MTU). She received her B. Eng. (2015) and M. Eng. (2018) from the School of Environmental Science and Engineering, Shanghai Jiao Tong University (SJTU), China. Her research interests focus on supercapacitors, capacitive deionization, and graphene synthesis and application.

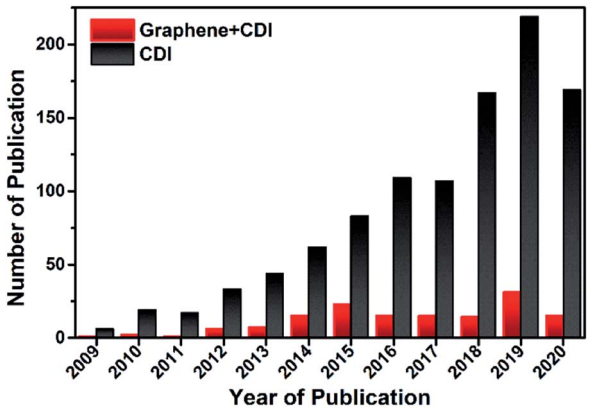

Fig. 1 Number of publications from 2009 to Aug 2020 when searching the keywords of "graphene & CDI" and "CDI" at web of science, respectively.

electrode materials,[14] and altering the operation model (*e.g.*, constant current *vs.* constant voltage[15] and intermittent flow *vs.* continuous flow[16]).

CDI by birth is seeking for high-surface-area electrodes. The screening of carbon materials has proved the feasibility of activated carbon (AC), mesoporous carbon (MC), carbon nanotubes (CNTs), carbon nanofibers (CNFs), and graphene as CDI electrodes. Among them, graphene, which possesses a surface-only structure and highly tunable properties, draws immense attention.[17] Since the first successful exfoliation in 2004, graphene has been widely applied in solar cells,[18–20] fuel cells,[21,22] batteries,[23–25] supercapacitors,[26–31] catalysis,[32] *etc.* The introduction of graphene to CDI occurred in 2009.[33] After that, both the CDI technology and the graphene-based CDI electrodes have experienced explosive progress (Fig. 1 and 2). The advantages of graphene toward CDI arise from its one-atom thick hexagonal crystalline carbon structure subsequent with large specific surface area, high electrical and thermal conductivities, and strong chemical stability.[34,35] However, graphene sheets easily aggregate to form a stacked one, which leads to the remarkably reduced accessible surface area for adsorption and postponed transfer of electrons and ions. Moreover, the high solution resistance and slow mass transport kinetics of the dilute salty solution for the CDI test (20–500 mg L^{-1}) make the negative influence more distinct.[36] To solve these issues, the development of structurally and chemically engineered graphene-based electrodes has become a rapidly growing research topic. This stimulates us to write this review for highlighting the progress in this important area, with emphasis on engineering graphene materials with desired functionalities. Three types of graphene materials, *i.e.*, 2D graphene, 3D porous graphene, and graphene/carbon composites, were systematically discussed with their electrosorption capabilities. Furthermore, it was shown that surface-modified graphene and composites of graphene with pseudocapacitive materials and battery materials overwhelmed the unmodified counterpart, achieving outstanding charge efficiency and ion selectivity.

Yun Hang Hu is the Charles and Carroll McArthur Endowed Chair Professor at Department of Materials Science and Engineering, Michigan Technological University. He is a fellow of American Association for the Advancement of Science (AAAS), American Chemical Society (ACS), American Physical Society (APS), American Institute of Chemical Engineers (AIChE), American Society of Metals (ASM), and Royal Society of Chemistry (RSC). He was elected as the chair of the Energy and Fuels Division of the American Chemical Society (ACS) in 2014 and the president of the Hydrogen Storage Division of International Association of Hydrogen Energy (IAHE) in 2015. He is the editor-in-chief of "Energy Science & Engineering" (Wiley journal) and an editorial board member for 8 international journals. His main research interests range from nanomaterials, clean fuels, solar energy, batteries, supercapacitors, and hydrogen storage materials to CO_2 conversion.

2. Basic principles of CDI

The studies on CDI traced back to the 1960s. Blair and Murphy proposed the concept of CDI and demonstrated the CDI model with AC electrodes for the first time.[37] As the investigation of CDI went further, CDI electrodes adopted the state-of-the-art carbon materials, *i.e.*, carbon aerogel (CA) in 1995, CNT in 2005, ordered mesoporous carbon in 2008, and graphene in 2009.[33,38–40] The rising interests in exploring CDI allow the development of CDI configuration, the setup of standard evaluation metrics, and the extension of ion storage mechanism from the electric double layer (EDL) to surface redox reaction and finally rocking-chair intercalation.

2.1 Development of CDI configuration

In the early 1960s, CDI was first reported as electrochemical demineralization, since it performed electrically induced ionic adsorption with a pair of porous "inert" electrodes.[37] In 1968, the long-term operation of CDI for a commercial purpose was demonstrated by Reid.[41] In 1971, Johnson *et al.* built an electrosorption model according to a capacitor mechanism and pointed out the importance of porous carbon electrodes with high surface areas for CDI.[42] In 1996, Farmer and co-workers stacked 192 pairs of carbon aerogel electrodes and removed 95% of NaCl from 4 liters of 100 μS cm^{-1} NaCl solution.[43]

In a conventional CDI cell, the charges are stored electrostatically in the EDLs formed at the surfaces of the porous electrodes. However, ion adsorption within the EDLs generally shows a poor charge efficiency, especially in the feed with high concentrations, due to the effects of counter-ion adsorption and co-ion expulsion coexisting at the electrode surface.[44,45] One feasible solution to alleviate the co-ion repulsion effect is to

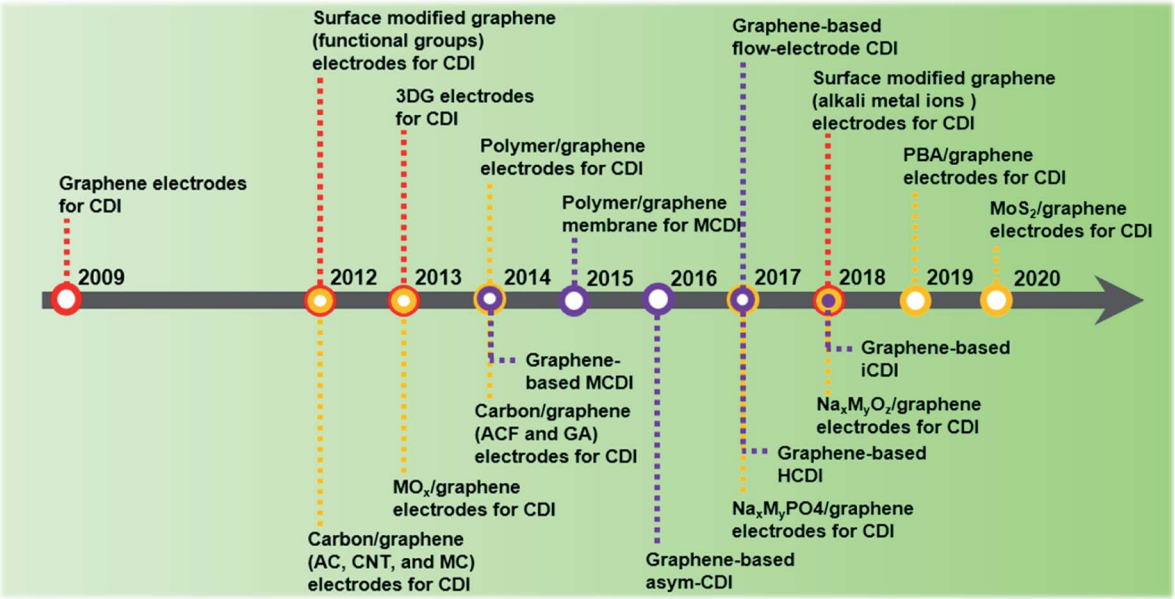

Fig. 2 A timeline diagram that represents the evolution of graphene-based electrodes and CDI configurations.

closely attach anion- or cation-exchange membrane to the electrode surface. Toward this end, Lee and co-workers pioneered a membrane-CDI (MCDI) system in 2006, and observed a significantly increased electrosorption efficiency of 92% compared to that of a traditional CDI system (77%).[46] Impressively, the charge efficiency of a MCDI system can be ~50% higher than that of a traditional one.[44,47–49] However, the insufficient contact between the polymeric ion-exchange membranes and the electrodes may generate considerable resistance for charge transport and ion diffusion, resulting in increased energy consumption and inhibited ion electrosorption.

Inspired by Na-ion batteries and capacitors, metal oxides/sulfides, sodium-containing metal oxides/phosphates, Prussian blue, *etc.* are introduced into CDI to enhance the electrosorption performance and suppress the inevitable oxidation of anodes.[50] The first desalination battery was promoted by Mantia and co-workers in 2012.[51] It comprised of two faradaic electrodes to capture cations and anions, respectively. Different from the capacitive ion storage at the surface or near the surface of electrode materials, rocking-chair ion intercalation occurs in the bulk of the materials. It brings about higher salt adsorption capacity (SAC), lower self-discharging, and lower energy consumption, yet the huge volume change induced by the bulk ion intercalation would weaken the electrode stability and thus reduce the lifetime.[52] In order to fabricate a stable CDI cell with improved electrosorption performances, Yoon and co-workers explored a hybrid CDI (HCDI) configuration comprising a capacitive electrode (attached by an anion exchange membrane) and a faradaic one.[53] The HCDI system presented an incredibly high SAC of 31.2 mg g^{-1}, compared to that of a conventional one (13.5 mg g^{-1}). It also exhibited excellent stability and rapid ion removal rate. Besides, Liu and co-workers developed an inverted-CDI (i-CDI) with capacitive carbon electrodes.[54] Impressively, the anions were held in the EDL that spontaneously formed at the anode surface modified by –COOH without external electric power, and could be released back to the electrolyte when applying an appropriate voltage. The inverted adsorption process stably performed over a surprisingly long duration of over 600 hours, ~530% longer lifespan than that of a conventional CDI cell.

Generally, a CDI electrode is fabricated by coating solvent-based electrode slurry on current collectors according to a recipe of porous active materials, conductive additives, and polymeric binders with a ratio approximate to 8 : 1 : 1.[55–57] The as-prepared electrodes commonly possess inherently high electrical and mass-transfer resistances due to insufficient contact between the carbon materials and the polymers.[43] Meanwhile, the susceptibility of polymeric binders to chemical attack and radiation damage shortens the lifetime of the CDI electrodes. In response to these issues, Kim and co-workers developed a novel flow-electrode CDI (FCDI) with two flow-electrodes (composed of AC suspension/NaCl solution) separated from the feed with porous separators.[58] In contrast to the static electrodes of conventional CDI, flow electrodes in FCDI conducted continuous desalination with infinite capacity and high removal efficiency. Also, they were regenerable during constant current discharging, in which 20% of the supplied energy was recovered. Moreover, Simon and co-workers displayed a suspension-electrode CDI (SCDI), where two suspension-electrodes separated by a porous separator flew through the polarized plates and was finally sieved from the activated carbon to produce a lower concentrated solution.[59] It is noteworthy that the electrical conductivity of the flowable electrodes is inferior to the static electrodes.[60]

2.2 Performance evaluation of CDI cells

A CDI cell comprises a pair of parallel electrodes and a separator between them, compacted with the current collectors and the

electrode supports. The separator (a woven/non-woven fabric, a polymeric mesh, or a glass fiber filter) and the electrode supports (fiberglass sheets) are usually electrically insulated, chemically inert, and anti-corrosive. To build a continuously recycling system that evaluates laboratory-scale CDI performance, the essential facilities include an electrolyte tank, a peristaltic pump, a conductivity meter, and an electrochemical workstation (Fig. 3A).[61] The peristaltic pump propels the constant flow of feed water from the electrolyte tank to the sealed CDI cell. Across the two electrodes, the potential difference applied by the electrochemical workstation with constant voltage or constant current mode can drive the cations in the feed water toward the negatively charged electrode and the anions toward the positively charged one. Ion storage on the electrodes *via* electrostatic adsorption, surface redox reaction, or rocking-chair intercalation accompanies with the change of the solution conductivity, which can be real-time recorded by the conductivity meter serially connected to the outlet.

CDI cells operate with either flow-by or flow-through mode according to the flowing directions of the feed water cross the charged electrodes (Fig. 3B).[23] The flow-through CDI with a perpendicular direction shows a faster response of deionization than the flow-by with a parallel path, as the latter requires additional diffusion time from the spacer channel to the electrodes. Otherwise, single-pass and batch-mode CDIs are distinguished depending on the cycling frequency of the feed water in the system.[62] The single-pass configuration, where the feed water travels from the electrolyte tank to the CDI cell just for once, is usually exploited for serial stacked CDI cells. In contrast, the batch-mode one, which allows the feed water recycling among the electrolyte tank and the CDI cell, is commonly used in laboratory evaluation based on a single cell.

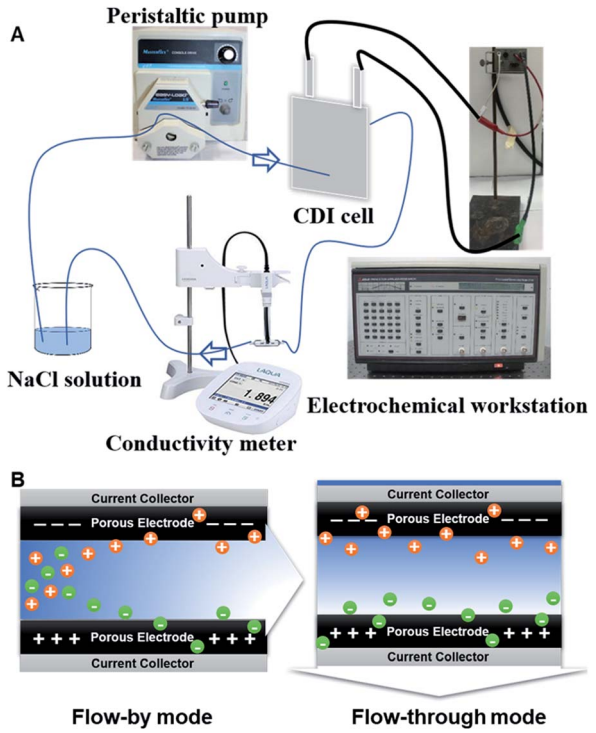

Fig. 3 (A) The recycling system of CDI. Reproduced with permission from ref. 61. Copyright 2018 Elsevier. (B) The illustration of flow-by and flow-through modes.

During the desalination process, the potential difference across the EDL is not allowed to exceed the water decomposition potential of 1.23 V based on the empirical theory, yet the voltage across the cell might exceed this threshold to compensate for the intrinsically systematic resistance of the cell, as long as the experiments are carefully observed to ensure no bubbles are generated in case of water electrolysis.[4,63,64] After the desalination process, the electrodes can be regenerated by shorting the circuit or reversing the polarity. The former is frequently reported since the adsorbed ions can be easily washed away by deionized water, whereas the latter shows high ion desorption rate but usually results in re-adsorption of released ions. A more effective method is to apply a low potential for a short time, which is expected to achieve faster equilibrium with mitigated re-adsorption effect.[65]

For a typical CDI test, when a constant voltage is applied to a CDI cell, the conductivity and the response current steeply decrease in the beginning and then gradually approach the equilibrium. In this process, applied voltages are generally in the range of 0.6–2.0 V. Increasing the applied voltages enhances the electrostatic force, resulting in higher adsorption capacity and rate within a relatively shorter equilibrium time.[66,67] The effect of salt concentration was also observed, namely, a concentrated salt solution has the lower system resistance and the more and thinner double layer formation.[68] In the lab-scale investigation, the massive deviation occurred in the initial concentration with the lowest one of 20 mg L^{-1} and the highest one of 23 376 mg L^{-1}. As the NaCl concentration increases, while scattered cases show a decrease in adsorption capacity,[67] the adsorption usually exhibited the Langmuir isotherms.[69,70] The influence of flow rate on CDI performance was also explored. A low flow rate can ensure the high removal ratio of salt at first, but prolong the adsorption duration. The variation of the flow rate from low (0.05–0.2 ml min^{-1}) to moderate (0.8–10 ml min^{-1}) values suggests higher amounts of ions in the cell per unit time, corresponding with a quicker and more evident transition to equilibrium. Further increase in the flow rate to an extremely high value would have negligible initial-changes in conductivity.[71] The flow rate employed in the lab-scale CDI tests is generally in the range of 2–100 mL min^{-1}.

Besides, a three-electrode configuration is widely applied for investigation of the fundamental electrochemical properties of electrode materials. With a working electrode, a reference electrode of Ag/AgCl (or calomel), and a Pt (or Ti) counter electrode, cyclic voltammetry (CV) and galvanostatic charge/discharge (GCD) can be attained to evaluate the adsorption behaviors of the cations and the anions, individually, on the electrode surfaces. Different adsorption behaviors can be observed owing to the varied practical sizes of the cations and the anions, and the distinct interactions between the ions and the material surfaces. It indicates that the electrosorption capacity of a CDI cell can be compromised with unfavorable ions. In other words, based on the analysis from a three-electrode cell, cathode and anode materials can be

rationally selected. In this light, an asymmetric CDI cell with remarkably improved electrosorption capacity and ion selectivity can be constructed.[72,73]

2.3 Ion storage mechanism

According to the type of the electrode materials, ions can be stored in CDI by three principal mechanisms, *i.e.*, electrostatic ion adsorption by porous carbon materials, surface redox reaction by pseudocapacitive materials, and rocking-chair intercalation by battery materials. For porous carbon materials, including AC, CNT, graphene, biomass-derived carbon, and metal–organic-framework-derived carbon,[74,75] the ion layering at the polarized electrode–electrolyte boundary and its vicinity creates an EDL.[76,77] The Gouy–Chapman–Stern double layer theory assumed that a double layer comprises an inner Helmholtz layer, an outer Helmholtz layer, and a diffuse layer. It discussed the double-layer capacitance (C_{dl}) in response to the surface area of electrode–electrolyte interfaces (S), charge separation distance (d), applied potential, and ion strength. Using the early Helmholtz model, which merely linked C_{dl} with S and d, the areal C_{dl} for a specific material can be estimated based on the equation: $C_{dl} = \frac{\varepsilon_0 \varepsilon_r S}{d}$ (ε_r is the relative permittivity of the electrolyte and ε_0 the vacuum permittivity of 8.854×10^{-12} F m^{-1}).[78] Under the assumption that d is ~1 nm, the areal capacitance of a porous carbon material is 5–20 μF cm^{-2}. Generally, a highly efficient CDI requires carbon materials with high hydrophilicity that allows effective contact between the ions and the electrode surfaces, high conductivity for rapid electron transfer, large accessible surface area for ion adsorption, suitable pore structure for electrolyte diffusion and ion storage, and good stability for long electrode lifetime.

Pseudocapacitive materials enable ion storage *via* a fast and reversible faradaic charge–transfer reaction. This capacitive-controlled reaction occurs at the surface or near-surface of suitable electrode materials. According to the traditional definition by B. E. Conway, surface functional groups, conductive polymers, and transition metal oxides/sulfides follow the pseudocapacitive mechanism for ion storage, and show (quasi-) rectangular CV curves and nearly linear GCD curves.[79] However, the discovery of intercalation pseudocapacitance makes it more complex to distinguish the pseudocapacitive materials. In the case of $LiCoO_2$, this typical battery material would show the pseudocapacitive characteristics when its particles are reduced to a critical dimension (6 nm).[80] Therefore, both the basic electrochemical properties and the electrochemical kinetics should be taken into account. As proposed by Dunn *et al.*, the analysis of CV curves can quantitively define the capacitive-controlled and the diffusion-controlled reactions.[81] In a simplified equation of $i(V) = av^b$, where i is current, V potential, and v scan rate, b with the valve of 0.5 suggests a battery behavior while b of 1 implies a capacitive property. Besides $LiCoO_2$, intercalation pseudocapacitance of $Ni(OH)_2$, TiO_2, Nb_2O_5, MoS_2, MoO_3, and Mxene have also been unraveled.[82]

Unlike the pseudocapacitive materials, the battery materials store ions *via* a diffusion-controlled reaction.[83] It displays at least a pair of redox peaks in the CV curve and detectable plateaus in the GCD curve. The faradaic redox reaction generally occurs at the peak or plateau potential, where the intercalation of cations (anions) into a lattice vacancy corresponds with a reduced (oxidized) lattice atom.[84] Commonly used battery materials, including $Ni(OH)_2$, TiO_2, Nb_2O_5, MoO_2, Mn_2O_3, Sn, *etc.*, can be classified as intercalation/deintercalation type, conversion type, and alloying type.[85] Toward desalination, battery materials show advantages over capacitive materials.[86] First, it possesses a higher theoretical capacity due to bulk redox reactions. Second, it rarely suffers from the co-ion effect and thus obtains enhanced charge efficiency. Third, it could achieve selective intercalation of ions with various dimensions and valences at different driving potentials. However, the battery materials show worse reversibility than carbon materials. The gradual decay of performance is observed even in the first several cycles unless the morphology and structure of materials are optimized.

2.4 Important parameters

In a recycling CDI system, electrosorption capacity (also termed as SAC) calculated from the changes of the conductivities during the adsorption can reflect the amount of salt removed by per unit gram of electrode materials.[43] Generally, electrosorption capacity is highly dependent on the properties of the electrode materials and the operational conditions of the CDI cell. For an electrode material, the surface area, pore structure, and surface functionalities should be well-controlled to get more active sites for adsorption.[87] In terms of the optimal operational conditions, initial concentration of the feed water, flow rate, temperature of the effluent, and applied potential between the two electrodes should be taken into consideration.[77,88] Substantially, electrosorption capacity is of the most importance in CDI and used to derive other three parameters. The first is the electrosorption rate (or average salt adsorption rate, abbreviated as ASAR), which indicates the adsorption capacity of ions within a certain period. The second is the cycling stability, which depicts the changes of the electrosorption capacity during the cyclic adsorption–desorption process. The last is the charge efficiency. As an indicator of energy efficiency, it accesses the ratio of equilibrium salt adsorption and total electrode charge.[89] The ideal charge efficiency has a value of 1, suggesting that supplying ions with one unit of charge to the electrode results in adsorption of oppositely charged ions with one unit of charge. However, in the case of EDL adsorption, coexistence of the counter-ions and the co-ions near the electrode surface remarkably reduces the overall efficiency. The consumed electrical energy due to the desorption of the co-ions could reach 30–35%. Common strategies adopted to improve the charge efficiency include alleviation of the co-ion effects with diluted feed water, and enhancement of the electrostatic force between the ions and the electrodes at a high potential or flow rate.[90,91] It is noteworthy that, although most works provided the electrosorption capacities and charge efficiencies of their CDI devices, it is not proper to evaluate the performance among these devices by merely comparing these numerical values due to the inconsistent calculation of electrode weights.

Table 1 The CDI performance of graphene electrodes[a]

Electrodes	CDI cell (anode// cathode)	Cell size (cm × cm)	NaCl concentration (mg L^{-1})	Flow frequency	Flow rate (ml min^{-1})	Voltage (V)	Time (min)	SAC (mg g^{-1})	ASAR (mg g^{-1} min^{-1})	Charge efficiency (%)	Ref.
rGO	rGO//rGO	—	22.5	B	40	2.0	30	1.85	—	—	33
Graphene nanoflakes (GNFs)	GNFs//GNFs	7 × 14	25	B	25	2.0	40	0.45	0.27[#]	—	96
GNFs	GNFs//GNFs	7 × 14	25	B	45	2.0	40	1.35	1.01[#]	—	97
Ultra-purified rGO	rGO//rGO	10 × 10	110[&]	B	10	2.0	7	3.54	—	—	98
rGO	rGO//rGO	—	25	B	—	2.0	120	0.88	—	—	99
Solar light rGO	rGO//rGO	—	5844	B	—	1.0	60	22.4	—	—	100
rGO	rGO//rGO	—	74	B	10	2.0	50	11.86	—	—	103
Oxygen-rich hierarchical porous graphene (O-PG)	O-PG//O-PG	—	500	B	25	1.4	60	21.1	~1.1[β]	—	104
CO_2 activated graphene (AGE-30)	AGE-30//AGE-30	4 × 3.5	500	B	10	1.2	30	6.26	—	0.56	105
Mesoporous graphene (mGE)	mGE//mGE	—	75	B	27	1.2	40	6.38	—	—	220
Graphene sponge (GS)	GS//GS	—	500	B	27	1.2	45	14.9	—	—	108
GH	GH//GH	—	500	B	10	2.0	320	49.34	—	—	64
GA	GA//GA	—		B	10	2.0	420	45.88	—	—	64
Graphene sheets with in-plane nanopores (NP-3DG)	NP-3DG//NP-3DG	—	500	B	—	1.6	50	15	—	0.3	109
HGF	HGF//HGF	6 × 4.5	572	B	15	2.0	60	29.6	—	0.35	36
3DMGA	3DMGA// 3DMGA	5 × 6	50	B	25	—	55	5.39	—	—	110
3DGA-OP	3DGA-OP// 3DGA-OP	—	500	B	6	1.2	120	14.4	~0.6[β]	—	113
Sponge-templated graphene (STGS)	STGS//STGS	—	50	B	2	1.5	60	4.95	—	—	112
Electrochemically activated graphene (ECAG)	ECAG//ECAG	—	87	B	10	1.8	8	14.25	2.01	0.83	115
SMG	SMG//SMG	3 × 4.5	50	B	10	2.0	30	9.13	—	—	116
HGC	HGC//HGC	3 × 4.5	295	B	10	2.0	30	14.08	—	0.2	117
3DG	3DG//3DG	—	70 (UO_2^{2+})	B	—	1.8	180	113.8	0.32	—	221
H_3PO_4 activated N-doped GA (PGA)	PGA//PGA	5 × 5	800	B	15	1.6	100	30.92	~0.8[β]	—	122
$-SO_3^-$-rGO	rGO//rGO	—	250	B	25	2	100	8.6	—	—	124
N-Doped graphene (NG)	NG//NG	—	50	B	27	1.8	40	4.81	—	0.46	126
N-Doped self-shrinking porous 3DG (NSPG)	NSPG//NSPG	4 × 4	100	B	15	2.0	30	13.16	—	—	127
Graphene nanosphere decorated N-doped layered mesoporous carbon frameworks	—	—	500	B	—	1.2	—	23.42	—	—	128
N-Doped carbon/rGO nano-sandwiches (NC/rGO)	NC/rGO//NC/rGO	—	589	B	100	1.2	30	17.52	—	—	129
Graphene-enriched N-doped carbonfibres (G/N-CFs)	G/N-CFs//G/N-CFs	9 × 9	585	B	7.7	1.2	30	27.6	—	—	130
N-Doped graphene sponge (NGS)	NGS//NGS	—	500	B	—	1.5	40	21	—	—	131
A carbon fibre cloth and sulphonated rGO composite (CFC-SRGO)	CFC-SRGO// CFC-SRGO	8 × 10	250	B	—	1.4	60	~8.2	—	~0.47	132
3D channel-structured graphene (CSG)	CSG//CSG	3 × 4.5	250	B	10	1.5	30	9.6	—	0.1	134
p-Phenylenediamine- or benzidine- functionalized graphene (DAB-mGO)	DAB-mGO// DAB-mGO	3 × 3	50	B	—	1.4	70	7.88	~0.24[β]	—	135
AC/triethyltetramine-modified GO (AC/TETA-mGO)	AC/TETA-mGO//AC/TETA-mGO	3 × 3	30	B	16	1.8	60	15.17	0.27	—	136
C-3D APGr and Q-3D APGr	C-3D APGr//Q-3D APGr	10 × 10	300	S	20	1.6	5	23.17		0.85	139
3DSGR or 3DNGR	3DNGR// 3DSGR	11.5 × 7.5	50	B	40	1.4	60	13.72	~0.4[β]	0.85	140
Highly-crumpled nitrogen-doped graphene (HCNDG)	HCNDG// HCNDG	7 × 14	25	B	25	2.0	40	1.96	—	—	222

Table 1 (*Contd.*)

Electrodes	CDI cell (anode// cathode)	Cell size (cm × cm)	NaCl concentration (mg L^{-1})	Flow frequency	Flow rate (ml min^{-1})	Voltage (V)	Time (min)	SAC (mg g^{-1})	ASAR (mg g^{-1} min^{-1})	Charge efficiency (%)	Ref.
Electrochemically nitrogen-doped graphene (ECNG)	ECNG//ECNG	—	87	B	10	1.2	6	18.6	—	—	223
Crumpled NG (CNG)	*CNG//CNG	—	200 (Pb^{2+})	B	100	1.2	5	521	—	—	224
—	—	—	200 (Cd^{2+})	—	—	—	—	498	—	—	
Pyrrolic N-dominated graphene (N-5-G)	N-5-G//N-5-G	2.5 × 2.5	93 (Pb^{2+})	B	—	1.2	30	259.5	—	—	225
B/N co-doped graphene xerogels (BNGXs)	BNGXs// BNGXs	6.5 × 3.4	800	B	20	1.6	50	18.45	—	0.45	226
N-Doped mesoporous carbon (NMC)	NMC//NMC	—	500	B	—	—	—	18.4	—	—	227

[a] (1) * represent membrane CDI, [#] rate constant from fitting data through pseudo first-order adsorption, [α] the constant current mode (unit: mA g^{-1}), and [β] the maximum salt adsorption rate. (2) S and B indicate the single-pass and batch-mode CDI. (3) [&] indicates conductivity (μS cm^{-1}), which is composed of 28.8 mg L^{-1} $CaCl_2$, 22.0 mg L^{-1} $MgSO_4 \cdot 7H_2O$, and 39.0 mg L^{-1} $NaHCO_3$. (4) [γ] corresponds with an areal unit of mg m^{-2}.

Calculation in most works are based on the weight of the active materials or all components (the active materials, the additives, and the binders) in both negative and positive electrodes. In some cases, however, the calculation is based on the weight of one electrode, which leads to doubled electrosorption capacity.[92]

Energy consumption and energy efficiency are also included in the metrics for evaluating a CDI system.[10,11] For a specific desalination process, energy consumption is equal to the input power multiplying by charging time with units of either joule (J) or kilowatt-hour (kW h). Normalized values per mole of salt removed or per unit operation time are mostly mentioned. Accordingly, energy efficiency is the minimum specific energy consumption of a thermodynamically reversible process divided by the specific energy consumption. In light of the irreversible entropic losses, the energy discrepancy between thermodynamic calculation and practical consumption cannot be negligible so far. Generally, systematical comparison of energy consumption and energy efficiency among different desalination technologies relies on the specific removal efficiency and water recovery. Removal efficiency or salt rejection describes the ratio of reduced concentration to the feed one in a desalination process. Higher removal efficiency is often achieved in a diluted salt solution at a high applied potential. Water recovery is described by a volume ratio of the desalinated water and the total water used in adsorption and desorption.

Apart from the electrosorption capacity and its derivatives, electrochemical impedance spectroscopy employs a frequency-dependent AC signal to characterize resistance and capacitive features of the electrodes and ion transport in the electrolytes. The two prevalent curves are Nyquist and Bode plots. The former plots the imaginary impedance against the real impedance, and the latter reflects the logarithm of the total impedance as well as the phase shift in response to the logarithm of the frequency.[93] By analyzing the EIS data, the contact resistance, diffusion resistance, and capacitance can be obtained to guide the modification of the electrode materials. Qu *et al.* demonstrated that the contact resistance between the current collector and the porous electrode was the principal source of series resistance in a CDI cell, and that the highly pressed counterpart possessed improved charge efficiency.[94] Lenz *et al.* observed EIS behaviors in an irregular, less densely packed carbon that gradually transferred from capacitance to mass transfer domination.[95] Thus, the EIS is commonly used as an auxiliary means in selection and design of electrode materials.

3. CDI cells with graphene electrodes

As an important component in a CDI cell, the electrode material attracts intensive research efforts due to their enormous influence on electrosorption performance (*i.e.*, SAC, ASAR, cycling stability, and charge efficiency) and energy efficiency. CDI cells with highly-efficient and long-lifespan electrodes would achieve bulk processing of saline water at high water recovery and salt rejection at the competitive cost of energy and infrastructure.

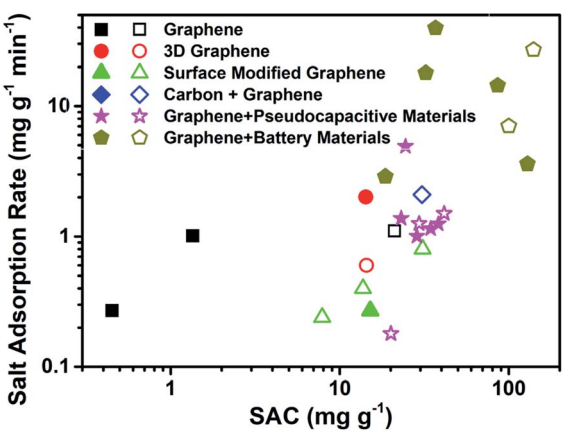

Fig. 4 The Ragone plot of representative graphene-based electrodes in Tables 1 and 2 (solid and open symbols correspond with average and maximum salt adsorption rates, respectively).

Graphene is a promising option for CDI with superb conditions for ion adsorption. Theoretically, single-layer graphene possesses a surface area of 2630 $m^2 g^{-1}$ and conductivity of 7200 S m^{-1}. However, the irresistible aggregation of graphene due to the strong van der Waals forces and π–π interactions between the planar planes dramatically reduces its effective surface area and thereby decreasing the electrosorption capacity. As unveiled by recent works (Table 1 and Fig. 4), structural engineering *via* construction of porous and three-dimensional (3D) architecture, and chemical engineering *via* surface doping and functionalization are potential options to solve this issue.

3.1 2D graphene electrodes

Early works on graphene-based CDI electrode materials mainly focused on synthesis of reduced graphene oxide (rGO) *via* the modified Hummers method followed by hydrazine reduction. In 2009, Pan and co-workers first fabricated the rGO electrodes for a batch-mode CDI in ~22.5 mg L^{-1} NaCl under voltages ranging from 0.8 to 2.0 V and observed an increase of SACs with the applied voltage.[33] The flower-shaped rGO possessed a small specific surface area (SSA) of 14.2 $m^2 g^{-1}$ and a maximum SAC of 1.85 mg g^{-1} at 2.0 V given the severe aggregation of graphene nanosheets. The following works in the same group promoted SSAs of rGO nanoflakes to 222 and 254 $m^2 g^{-1}$, yet the resulted SACs remained 1.35 mg g^{-1} (~25 mg L^{-1} NaCl, 2.0 V) and 0.5 mg g^{-1} (~20 mg L^{-1} $FeCl_3$, 2.0 V), respectively.[96,97] While further purification of rGO with H_2O_2 and HCl slightly increased the SAC to 3.54 mg g^{-1} in feeding water containing $CaCl_2$, $MgSO_4$, and $NaHCO_3$,[98] the electrosorption behavior of graphene materials is still far below that of its carbon relatives.[99]

Great efforts have been made to improve the ion adsorption capacity and transport kinetics of graphene materials. The surging SAC to 6.26–22.4 mg g^{-1} in rGO electrodes was mainly attributed to the modification in the microstructure (*e.g.*, curve morphology and in-plane porous structure) and surface functionalities (*e.g.*, oxygen functional groups). The practical strategies include the novel reduction process (*i.e.*, solar irradiation and thermal shock reduction),[100,101] the bottom-up synthesis (*i.e.*, Fe-catalyzed glucose-flowing method),[102] and post-treatment with KOH, HNO_3, and CO_2.[103–105] For example, the solar irradiation reduction can allow us to show the "process–property relationship" in 2D graphene electrode. With solar light focusing on GO, the sudden increase in temperature made GO decomposed into graphene, CO_2, and marginal H_2O. Then, the pressured CO_2 induced the rapid exfoliation of the graphene, leading to its structure transition from dense to fluffy. The as-prepared graphene with folded and wrinkled structure, which can maintain the high surface area of the electrode, achieved a high SAC of 22.4 mg g^{-1} in 5844 mg L^{-1} NaCl solution at 1 V.[100] Additionally, 3D porous graphene and surface-modified graphene discussed in the following part are regarded as better solutions.

3.2 3D porous graphene electrodes

3D porous graphene is a self-supported and anti-aggregated form of 2D graphene. The interconnected porous 3D framework self-assembled with randomly-oriented wrinkled graphene sheets can provide larger accessible surface areas and shorter diffusion distance for ions.[27,106,107] Thus, 3D porous graphene with a sponge-like structure achieved 3.2 times larger electrosorption capacity at 1.2 V in 500 mg L^{-1} NaCl solution (14.9 mg g^{-1} *vs.* 4.64 mg g^{-1}) and nearly twice larger one at 1.5 V in 50 mg L^{-1} NaCl solution (5.52 mg g^{-1} *vs.* 2.36 mg g^{-1}) than pristine graphene (PG) with a planer structure.[108] Besides, the electrosorption performance of 3D porous graphene can be further enhanced through modification on surface wettability and pore structure. Yu and coworkers proposed a water-enhanced mechanism and demonstrated the facilitated ion transport on a hydrophilic surface.[64] Yang and coworkers attested that the introduction of in-plane pores could not only increase the SSAs from 247 to 445 $m^2 g^{-1}$ but also promote the methylene blue adsorption with the changes of solvated surface areas from 730 to 1060 $m^2 g^{-1}$.[109] It suggests the quick access of ions to the accessible surface and accordingly elevated desalination ability. All of the desired features for CDI can be integrated in a hole-rich graphene framework (HGF).[36] By etching the carbon atoms on the basal plane of GO with a chemical activator of H_2O_2, hole-rich GO (HGO) was produced as the precursor for HGF (Fig. 5A). The obtained HGF, as statistics revealed in the area of 0.1 mm^2, presented 217 micropores, 89 mesopores, and 2 macropores on a graphene sheet (Fig. 5B). The abundant holes endowed HGF to hold a large surface area (124 $m^2 g^{-1}$) for ion adsorption over GF (91 $m^2 g^{-1}$), an oxygen-rich surface for favorable wettability, and more pathways for fast electrolyte transport. Thus, HGF achieved highly efficient desalination with SACs of 8.0, 16.9, and 29.6 mg g^{-1} at 2.0 V in the NaCl solution with initial concentrations of 80, 270, and 572 mg L^{-1}, respectively (Fig. 5C). High SAC was observed in high salinity solution due to the low solution resistance and short

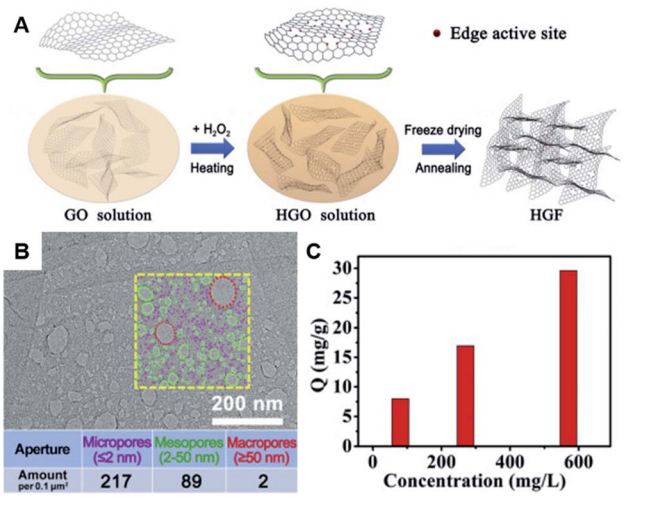

Fig. 5 (A) Schematic depicting the fabrication process of HGF. (B) TEM images of HGO sheet. (C) The electrosorption capacity of HGF in NaCl aqueous electrolyte with different concentrations (80 mg L^{-1}, 270 mg L^{-1}, and 572 mg L^{-1}) at 2.0 V. Reproduced with permission from ref. 36. Copyright 2018 Elsevier.

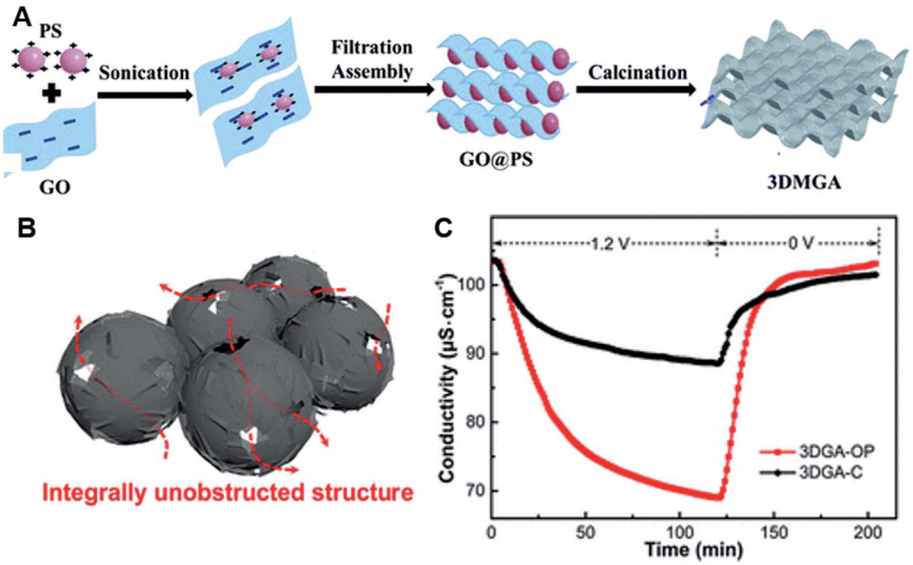

Fig. 6 (A) Schematic illustration of the 3DMGA preparation. Reproduced with permission from ref. 110. Copyright 2013 The Royal Society of Chemistry. (B) Schematic of ion transport in 3DGA-OP during the capacitive deionization process. (C) Solution conductivity *vs.* time curves for 3DGA-OP and 3DGA-C electrodes in a 50 mg L^{-1} NaCl solution. Reproduced with permission from ref. 113. Copyright 2020 American Chemical Society.

diffusion distance, accompanied with high initial current, fast falling rate, and short adsorption equilibrium in the CDI test.

In contrast to the self-assembly method, the sacrificial-template-directed method shows advantages in controlling and reserving the dimension, topography, and macropore distribution of the as-fabricated 3D graphene. Generally, a sacrificial template is well mixed with graphite oxide through sonication[110,111] or simple immersing,[112] then calcined to form the 3D architecture. Commonly applied sacrificial templates include polystyrene (PS),[110] SiO_2 spheres,[111] MnO_2,[72] and even sponge.[112] Taking 3D macroporous graphene architecture (3DMGA) as an example, the electrostatic assembly of positively charged GO and negatively charged PS and the following pyrolysis of PS produced a unique porous network with intact continuous walls (Fig. 6A). The well-reserved macrostructure provided an efficient buffer for electrolytes. However, in a NaCl aqueous solution with an initial conductivity of 105 mS cm^{-1}, the SAC of 3DMGA electrodes at 1.2 V was only 1.97 mg g^{-1} because the locally closed structure isolated those as-formed pores from each other, leading to postponed electrolyte diffusion.[110] To break the encapsulated character, Zhu *et al.* substituted the large-sized GO sheets with fragmented GO sheets (Fig. 6B). The intentionally designed incomplete graphene-based spherical hollow shells possess open and interconnected porous architectures (3DGA-OP) ideal for ion adsorption. Thus, the 3DGA-OP achieved an electrosorption capacity of 7.14 mg g^{-1} and a salt adsorption efficiency of about 56% at 1.2 V in 50 mg L^{-1} NaCl solution (Fig. 6C), far exceeding its counterpart with typically isolated pore structure (2.65 mg g^{-1}, 41%).[113] This well-defined and interconnected 3D macro/mesostructure can be replicated from a 3D template as well. Self-assembled silica opal microballs, polyurethane sponge, and Ni foam are perfect templates for the production of 3D graphene with excellent adsorption capability.[112,114,115]

Admittedly, 3D graphene has a favorable structure for fast and efficient ion adsorption. However, stacked graphene sheets, affluent defects, and oxygen functional groups may deteriorate the accessible surface area and electrical conductivity of the GO-assembled 3DG. In contrast, light, high-quality, and self-supported 3D graphene from a template-directed chemical vapor deposition showed limited application potential in CDI owing to its high cost and small dimension ($298 for a piece of 2 cm × 2 cm, MTI Cooperation, USA). In this regard, a series of new chemistries between alkali metals (or their oxides) and carbon oxides were developed by Hu and coworkers to fabricate low-cost and high-quality 3D porous graphene. With Na chemistry, surface microporous graphene was synthesized after heating at 550 °C for 12 h in the CO_2 atmosphere.[116] The dual functions of CO_2 were unraveled. CO_2 not only reacted with Na to produce graphene and $NaCO_3$, but also interacted with the graphene surface to yield micropores. The as-obtained surface microporous graphene (SMG) exhibited a flower-like morphology with a channel width ranging from 300 nm to 1 μm. On the surface of the graphene walls, the micropores formed *in situ* were homogeneously distributed with the average width of 1.8 nm (Fig. 7A). Impressively, these micropores possessed a deepness of ~0.1 nm, much smaller than the thickness of the three-layer graphene walls (1.1 nm), indicating that the micropores were only distributed on the surface. The surface micropores allowed direct contact with the buffered electrolyte in the macropores and thus improved electrolyte transport in a micropore-dominated material. Thereby, SMG achieved a SAC of 9.13 mg g^{-1} at 2.0 V in 50 mg L^{-1} NaCl solution over AC (3.46 mg g^{-1}) (Fig. 7B). Besides, the

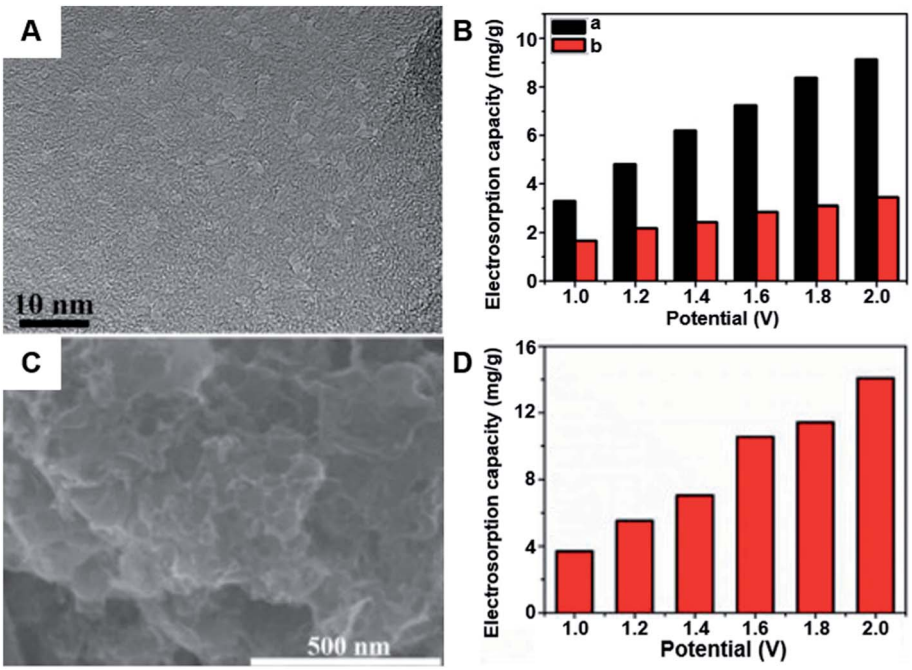

Fig. 7 (A) STEM image of surface-microporous graphene. (B) Electrosorption capacity of surface-microporous graphene (a) and activated carbon (b) in 50 mg L^{-1} NaCl aqueous solution. Reproduced with permission from ref. 116. Copyright 2019 Elsevier. (C) SEM image and (D) electrosorption capacities of HGC. Reproduced with permission from ref. 117. Copyright 2019 Elsevier.

exploitation of the reaction between Li and CO at 400 °C for 24 h resulted in honeycomb graphene clusters (HGC), which showed a large surface area of 1962 m^2 g^{-1} and a mesostructure with pores concentrated on 5–10 nm and 40 nm (Fig. 7C).[117] These mesopores provided mostly surface sites (1758 m^2 g^{-1}) for ion adsorption and functioned as electrolyte reservoirs for fast ion transport, which allowed a SAC of 14.08 mg g^{-1} in 295 mg L^{-1} NaCl solution at 2.0 V (Fig. 7D). As discussed above, these new chemistries not only provide a brand-new option for constructing 3D graphene, but also exhibit enormous potential for scalable production due to the simple apparatus and the mild reaction conditions. Moreover, emerging attention has been drawn for this synthesis route, and new chemistries have been unraveled, such as Mg + CS_2, Li + CS_2, Mg/Zn + CO_2, *etc.*[118–120]

3.3 Surface-modified graphene electrodes

Graphene regulation through heteroatom doping/substitution is beneficial for adsorption capability, charge efficiency, and long-term performance of CDI. Principally, non-metallic elements (O, N, P, and S) can amend electrolyte diffusion and ion migration in the pores, alter the interaction between ions and the graphene surface, and alleviate the co-ion expulsion and carbon oxidation.[121–124] Oxygen functional groups in the form of carboxyl, carbonyl, hydroxyl, quinone, and lactone can improve the wettability of the graphene surface. Due to the chelating effect, oxygen shows a strong interaction with alkaline-earth metals.[104,125] GO reduction or graphene activation with the base or acid solution and CO_2 gas is the main source of oxygen. However, the negative influence of oxygen on electrical conductivity is considerable, particularly for large amounts of oxygen on the surface. Alternatively, nitrogen doping enhances the hydrophilicity and the conductivity of graphene materials. Both chemical nitrogen, such as functional groups of amino and nitrite, and structural nitrogen, like pyrrolic, pyridinic, and graphitized nitrogen, can enhance CDI performance.[126–129] The doping level of N in individual graphene is generally below 10 at%, but it would reach 20 at% in the carbon/graphene composites.[130] Impressively, nitrogen-doped GS (NGS) showed a remarkable enhancement in electrosorption capacity (21.0 mg g^{-1}), which was about 1.4 and 4.6 times larger than GS and PG, respectively (Fig. 8A).[131] The hydrophilic sulfonic group (–SO_3H) endowed graphene with decreased contact angle from 73.7 to 39.5° (Fig. 8B, inset). The strongly negatively charged graphene with –SO_3H repelled each other, and the homogeneously dispersed graphene received a 109% increase in electrosorption capacity with a salt removal efficiency of 83.4% (Fig. 8B).[123] More importantly, tuning the content of –SO_3H groups on the rGO backbone (SrGO) can promote the passage of cations with prohibiting anions. The SrGO-decorated carbon fibre cloth (CFC) behaved like a cation-exchange-membrane-coupled one with comparable charge efficiency. Furthermore, the ion selectivity of CFC–SrGO composites was observed in a NaCl solution with high ionic strength. The 100% charge efficiency in a solution with a conductivity of 100 mS cm^{-1} dropped to 10% for CFC and comparably 40% for CFC–SrGO when the conductivity elevated to 2000 mS cm^{-1}.[132] The ion selectivity is also dependent on its affinity with functional groups. The thiol groups (–SH) in GO/AC composites provided higher removal capacity of Pb^{2+} over Ca^{2+} and Mg^{2+}.[133] Apart from non-metallic elements, metallic element doping can reduce the charging resistance and

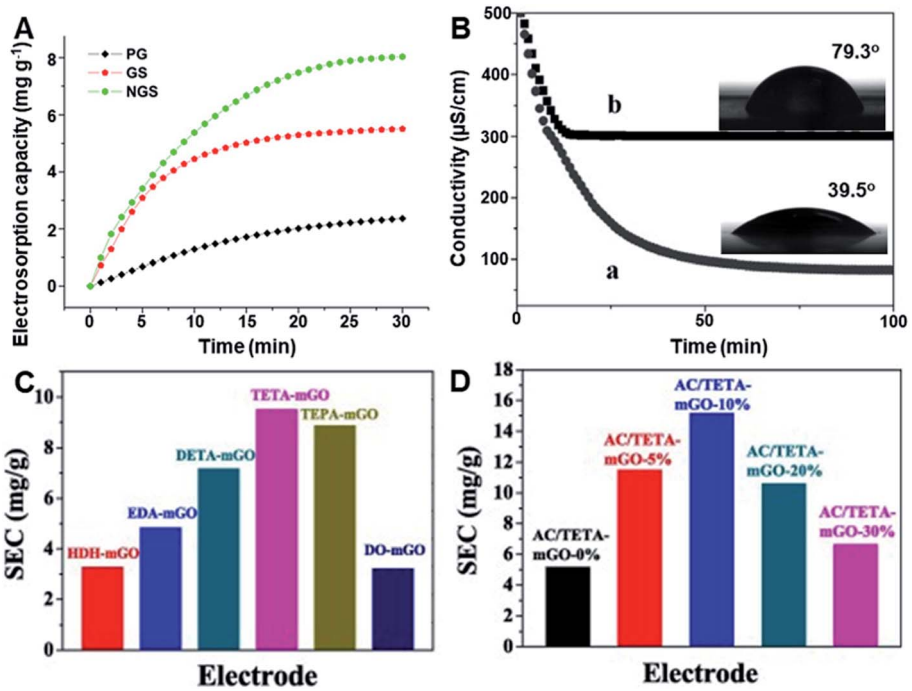

Fig. 8 (A) Electrosorption capacity for NGS, GS and PG electrodes over 30 minutes in NaCl solution with an initial concentration of ~50 mg L^{-1} at an applied voltage of 1.5 V. Reproduced with permission from ref. 131. Copyright 2015 Springer Nature. (B) Electrosorption of Na^+ on electrodes based on (a) sulphonated and (b) unsulphonated GNS (insets are the contact angle of water droplet on unsulphonated (upper) and sulphonated (lower) graphene film). Reproduced with permission from ref. 123. Copyright 2012 Elsevier. (C and D) Electrosorption capacity of mGO with HDH (hydrazine hydrate), EDA, DETA, TETA, TEPA, and DO (1,8-diaMinooctane) (C), and AC/TETA-mGO with different ratio (D) in NaCl solution with the initial conductivity of ~127 μS cm^{-1}. Reproduced with permission from ref. 136. Copyright 2020 Elsevier.

enhance the electrochemical properties. It has been demonstrated by 3D channel-structured graphene with K^+ intercalation, which achieved SACs of 5.70 and 9.60 mg g^{-1} in 50 and 295 mg L^{-1} NaCl aqueous solutions, respectively, after applying a voltage of 1.5 V for 30 min[134] Besides, functionalization of graphene can exploit small organic molecules. The SAC of *p*-phenylenediamine- or benzidine- (DAB) modified graphene (DAB-mGO) for Na^+, Mg^{2+}, Ca^{2+} was ~1.3–1.5 times higher than that of AC. SACs at 1.4 V were presented in a descending order: Ca^{2+} (13.55 mg g^{-1}) > Mg^{2+} (8.02 mg g^{-1}) > Na^+ (7.88 mg g^{-1}).[135] Furthermore, the investigation in a series of ethylene amines suggested that the enhanced conductivity arose from the interfacial interaction between the electrons and the salt ions, and the reaction between $-NH_2$ groups and the oxygen-containing groups of GO created a porous nanostructure.[136] Triethyltetramine (TETA) surpassed ethylenediamine (EDA), diethyltriamine (DETA), and tetraethylpentylamine (TEPA), allowing the modified graphene oxide (mGO) or AC/graphene composites to show the highest specific capacitance in three-electrode tests and the highest SAC in NaCl solution with initial conductivity of ~127 μS cm^{-1} (Fig. 8C and D).

What is more, the potential of zero charge (pzc), at which the least electrosorption capability of ions takes place, can describe the electrochemical properties of surface-functionalized graphene. Relative to pzc of the pristine graphene surface, the graft of carboxyl and hydroxyl leads to a negative shift of pzc, whereas the amine groups push forward a positive movement. This allows one to evaluate the working windows and thus ion selectivity, both of which are essential for constructing an asymmetrical CDI with the rational cathode and anode.[137,138] Based on surface-modified 3D activated porous graphene (3D APGr), Choi and coworkers demonstrated an asymmetrical CDI cell that achieved an outstanding SAC of 23.17 mg g^{-1} at 1.6 V when 300 mg L^{-1} NaCl solution flowed by a single-pass CDI at a rate of 10 mL min^{-1}.[139] While the ultra-high surface area (2680 m^2 g^{-1}) and hydrophilic surface (contact angle of approximately 88.3°) of 3D APGr contributed to ion adsorption, the superb CDI performance mainly arose from the graphene cathode and anode modified with carboxymethyl cellulose (C-3D APGr) and quaternary ammonium cellulose (Q-3D APGr), respectively (Fig. 9A). The resulting negatively charged (COO^{2-}) and positively charged (NR^{4+}) surfaces, which showed ion selectivity for Na^+ and Cl^-, respectively, exhibited better hydrophilicity as contact angles decreased to 26° and 28°. The alleviated co-ion repulsion effects allowed the asym-QC-3D APGr (Fig. 9B) to display overwhelming electrosorption capacity, charge efficiency, and cycling stability over symmetrical CDI with 3D graphene (3DGr), 3D porous graphene (3DPGr), and 3DAPGr (Fig. 9C). Analogously, the ion-selective coating can be sulfonic and amine functional groups grafted on 3DGR (3DSGR or 3DNGR) using an aryl diazonium salt solution and 3-aminopropyltriethoxysilane, respectively.[140] The regulation of co-ion movement and the increase of wettability ensured a SAC of 13.72 mg g^{-1} and correspondingly charge efficiency of 0.85 at

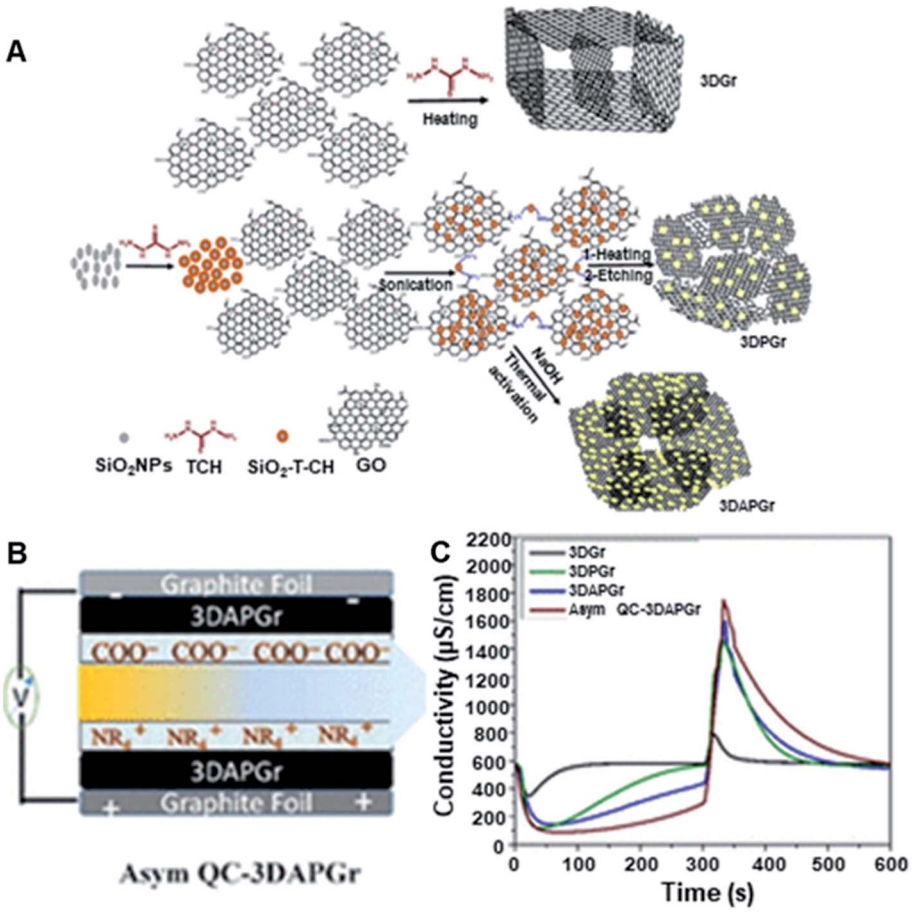

Fig. 9 (A) Fabrication of highly nanoporous graphene. (B) Schematic diagram for asym-QC-3DAPGr CDI cell. (C) Desalination plot for the synthesized electrode materials at 1.4 V with flow rate of 20 mL min^{-1}. Reproduced with permission from ref. 139. Copyright 2016 American Chemical Society.

1.4 V in 500 mg L^{-1} NaCl aqueous solution. Besides, the surface of 3DG amended with ethylenediaminetetraacetic acid (EDTA) served as a cathode in asymmetrical CDI and thus attained high removal efficiencies for Na^+ (98.7%) and Pb^{2+} (99.9%) simultaneously, owing to the chelation adsorption of Pb^{2+} on EDTA and electrostatic adsorption of Na^+ on the graphene surface.[141]

4. CDI cells with graphene-based composite electrodes

In graphene-based composites, carbon-based materials, pseudocapacitive materials, and battery materials display dual functions in facilitating CDI performance, (1) as spacers for alleviating agglomeration and restacking of graphene and (2) as additional active sites for ion adsorption (Table 2 and Fig. 4).[142]

4.1 Carbon/graphene composite electrodes

Ever since CDI technology was proposed, AC, MC, CNTs, CA, and activated carbon fibers (ACFs) have been deemed as the essential CDI electrode materials. When incorporating with graphene, these carbon materials can function as either intercalated spacers or frameworks. The obtained carbon/graphene composites show an increase in their effective surface areas, electrical conductivity, mechanical strength, chemical stability, *etc.*[143,144]

Intercalation of ACs, carbon spheres, or CNTs into the interlayers of graphene builds a typical architecture for carbon/graphene composites.[145–147] 3D hierarchical porous rGO/AC composites prepared by a microwave-assisted method displayed excellent desalination behavior.[148] The most impressive factor in this reaction is the multiple roles of ethylene glycol (EG) (Fig. 10A). It served as the solvent and microwave absorber to realize homogeneous dispersion and rapid heating of the AC–GO mixture. The high-temperature EG, which allowed quick reduction of GO to rGO, uniform dispersion of rGO on the AC surface, and formation of local hot spots and bubbles, induced a particular structure where wrinkled rGO sheets were interlaced with AC-p (Fig. 10B and C). Moreover, based on the contact angle dropping within 20 s, EG was demonstrated to be a wettability enhancer as rGO/AC-p electrode showed sharply decreased contact angle from 90° to 66° while AC-p electrode exhibited slightly decreased one from 127° to 113.1° (Fig. 10D). The obtained rGO/AC-p electrode displayed large SSA (2759 m^2 g^{-1}) and electroactive surface area (3.47 cm^2 mg^{-1}), which endowed the SAC to reach 18.6 ± 1.2 mg g^{-1} with charge

Table 2 The CDI performance of graphene composite electrodes[a]

Electrodes	CDI cell (anode//cathode)	Cell size (cm × cm)	NaCl concentration (mg L^{-1})	Flow frequency	Flow rate (mL min^{-1})	Voltage (V)	Time (min)	SAC (mg g^{-1})	ASAR (mg g^{-1} min^{-1})	Charge efficiency (%)	Ref.
Graphene/CNTs/ACs (GTAC)	GTAC//GTAC	—	50	B	27	1.2	40	2.3	—	0.53	143
AC/*m*-phenylenediamine (mPEA)	AC/mPEA//AC/mPEA	8 × 8	117	B	16	1.8	40	11.8	—	—	144
Graphene/CNTs sponge (GNS)	GNS//GNS	—	500	B	27	1.2	—	18.7	—	0.55	154
rGO/AC (GAC)	GAC//GAC	8 × 10	25	B	25	2.0	65	0.85	—	—	145
Graphene-coated hollow mesoporous carbon spheres (GHMCSs)	GHMCs//GHMCs	5 × 6	34	B	25	1.6	120	2.3	—	—	146
CNTs-rGO	CNTs-rGO//CNTs-rGO	—	50	B	25	1.6	60	0.33	—	0.4	147
rGO/AC	rGO/AC//rGO/AC	8 × 5	100	B	12	1.2	30	18.6	—	0.69	148
Carbon nanoparticles decorated graphene sheets (CN-GS)	CN-GS//GN-GS	—	500	B	—	1.4	60	30.7	~2.1[β]	—	149
N-rGO/CNTs	*N-rGO/CNTs//N-rGO/CNTs	—	2500	B	50	±1.4 (100)[α]	100	75	—	—	150
3D mesoporous graphene sheet-sphere (MGSS)	MGSS//MGSS	—	500	B	—			22.9	—	—	151
3D graphene-based hierarchically porous carbon (3DGHPC)	3DGHPC//3DGHPC	5 × 5	25	B	30	1.2		6.18	—	—	111
GO/resorcinol–formaldehyde microsphere (GORFM)	GORFM//GORFM	6 × 4	800	B	20	1.8	40	33.52	—	0.7962	152
G@MC-O-thin	G@MC-O-thin//G@MC-*O*-thin	5 × 10	500	B	25	1.5	120	24.3	—	~0.7	153
Graphene (GR)/CNTs	GR/CNTs//GR/CNTs	—	25	B	25	2.0	120	1.41	—	—	155
CNTs/graphene (G)	CNTs/G//CNTs/G	—	780	B	25	2.0	30	26.42	—	—	156
SWCNTs/rGO	SWCNTs/rGO//SWCNTs/rGO	—	300	B	10	2.0	600	48.73	—	0.15	157
rGO/ACF	rGO/ACF//rGO/ACF	—	100	B	5	1.2	30	9.2	—	0.328	158
rGO/ACF	rGO/ACF//rGO/ACF	4.5 × 5.5	400	B	15	1.2	30	7.2	—	—	159
GO-embedded porous carbon nanofiber (PCNF)	GO-PCNF//GO-PCNF	—	100	B	6	1.2	125	7.8	—	—	160
Graphene-composite carbon aerogels (GCCAs)	GCCAs//GCCAs	—	500	B	25	1.5	600	26.9	—	—	162
rGO–carbon aerogels (CAs)	*rGO-CAs//rGO-CAs	—	50	B	40	1.2	30	—	—	0.52	163
AC-rGO	AC-rGO//AC-rGO	—	250	S	30	1.5	3	~0.005[γ]	—	—	228
Cellulose acetate (CA)–rGO	CA-rGO//CA-rGO	5 × 5	50	B	8	1.5	57	5.6	—	—	229
Graphene/mesoporous carbon (GE/MC)	GE/MC//GE/MC	7 × 8	40	B	25	2.0	65	0.731	—	—	230
GO/auricularia-derived hierarchical porous carbon (H2)	H2//H2	—	55.72	B	—	1.2	60	7.74	—	—	231
	—	—	200	B	—	—	—	18.07	—	—	
N-Gr/CNT	N-Gr/CNT//N-Gr/CNT	—	500	B	12	1.2	60	25.74	—	—	232
Microporous carbon spheres (MCS) decorated 3DGF(3DGF-MCS)	3DGF-MCS//3DGF-MCS	—	500	B	100	1.2	25	19.8	—	0.5	233
3D rGO-melamine formaldehyde composites (3D RGO-MF)	3D RGO-MF//3D RGO-MF	5 × 5	500	B	—	2.0	300	21.93	—	—	234
N-Doped hollow mesoporous carbon sphere/HGH (N-HMCS/HGH)	N-HMCS/HGH//N-HMCS/HGH	—	500	B	25	1.4	120	17.8	—	—	235

Table 2 (*Contd.*)

Electrodes	CDI cell (anode//cathode)	Cell size (cm × cm)	NaCl concentration (mg L^{-1})	Flow frequency	Flow rate (mL min^{-1})	Voltage (V)	Time (min)	SAC (mg g^{-1})	ASAR (mg g^{-1} min^{-1})	Charge efficiency (%)	Ref.
SiW_{12}@PANI/EGC	SiW_{12}@PANI/EGC// SiW_{12}@PANI/EGC	2 × 2	500	B	—	1.2	40	23.1	1.38	—	136
GO/PPy	*GO/PPy//GO/PPy		200	B	20	1.2	10	88.43	—	—	170
PPy/GO	PPy/GO//PPy/GO	—	100 (Cu^{2+})	B	—	1.2	40	41.51	~1.5$^{\beta}$	—	171
MnO_2-NRs@graphene	MnO_2-NRs@graphene// MnO_2-NRs@graphene	—	50	—	—	1.2	120	5.01	—	—	176
Graphene–chitosan–Mn_3O_4 (Gr-Cs-Mn_3O_4)	Gr-Cs-Mn_3O_4// Gr-Cs-Mn_3O_4	4 × 4	250	B	10	1.6	120	14.83	—	—	177
rGO–SnO_2	rGO–SnO_2// rGO–SnO_2	2.5 × 2.5	400	B	10	1.2	30	17.62	—	—	178
RGO@Fe_3O_4	RGO@Fe_3O_4// RGO@Fe_3O_4	—	250	B	30	1.2	30	8.33	—	~0.85	179
GO/TiO_2 nanorod	*GO/TiO_2 nanorod//GO/TiO_2 nanorod	10 × 10	300	S	20	1.2	5	16.4	—	0.69	180
CeO_2/rGO nanoflake (NF)	CeO_2/rGO NF// CeO_2/rGO NF	5 × 5	121	B	15	1.4	55	17.7	—	—	181
ZrO_2-doped GO	ZrO_2-doped GO// ZrO_2-doped GO	—	50	B	—	1.2	2	6.3	—	0.84	182
Graphene/CNTs/ZnO (FGC-ZnO)	FGC-ZnO//FGC-ZnO	5 × 5	600	B	10	1.2	120	28.62	1.004	—	183
α-MnO_2/G-2	G//α-MnO_2/G-2	11 × 5.5	100	B	10	1.2	100	29.5	~1.25$^{\beta}$	—	184
RGO–PPy–Mn	RGO–PPy–Mn// RGO-PPy-Mn	5 × 5	500	B	10	2.0	120	18.4	—	—	185
Graphene/SnO_2 (Gr/SnO_2)	Gr/SnO_2//Gr/SnO_2	—	30	B	—	1.4	90	1.49	—	—	186
rGO–TiO_2	rGO–TiO_2//rGO–TiO_2	5 × 5	75	B	15	1.2	18	24.58	—	—	187
rGO/TiO_2 nanotubes (rGO/TiONTs)	rGO/TiONTs// rGO/TiONTs	—	15 000	B	—	1.2	30	104.29	—	0.98	188
N-Doped graphene quantum dots decorated onto halloysite nanotubes (N-GQDs@HNTs)	N-GQDs@HNTs// N-GQDs@HNTs	4 × 4	500	B	20	1.2	60	20.1	0.18	—	189
GA/TiO_2	GA/TiO_2//GA/TiO_2	—	500	B	—	1.2	7	15.1	—	0.68	190
Mn_3O_4/RGO	RGO//Mn_3O_4/RGO	8 × 4	1000	B	5	1.2	60	34.5	1.15		192
Fe-rGO@AC	Fe-rGO@AC//Fe-rGO@AC	—	16 (As(v))	B	50	1.2	120	~10.5	—	—	193
$MnFe_2O_4$/porous rGO (MFO/PrGO)	MFO/PrGO//rGO	—	50	B	100	1.6	~33	8.9	—	—	194
$MnFe_2O_4$–rGO (MFO–rGO)	MFO–rGO// MnO_2–rGO	—	—	B	—	—	—	38.28	1.248	—	195
CuAl-LDO/rGO	CuAl-LDO/rGO// rGO	—	1000	B	—	1.2	60	64	—	—	196
MgAl-Ox/G	MgAl-Ox/G/AC-HNO_3	5 × 6	500	S	10	1.0	10	13.6	—	0.887	197
NiCoAl-LMO/rGO	NiCoAl-LMO/rGO//H-AC	—	500 (NaF)	S	9	1.4	15	24.5	4.9	—	198
Etching Fe_3O_4 nanoparticles grown on graphene sheets (E-Gr-Fe_3O_4)	E-Gr-Fe_3O_4//E-Gr-Fe_3O_4	4 × 4	150	B	10	1.6	120	10.3	—	—	236
Chemically exfoliated MoS_2 (ce-MoS_2)	AC//ce-MoS_2	1.5	23 376	B	—	1.2	90	8.81	—	—	200

Table 2 (*Contd.*)

Electrodes	CDI cell (anode// cathode)	Cell size (cm × cm)	NaCl concentration (mg L^{-1})	Flow frequency	Flow rate (mL min^{-1})	Voltage (V)	Time (min)	SAC (mg g^{-1})	ASAR (mg g^{-1} min^{-1})	Charge efficiency (%)	Ref.
MoS_2/rGO	AC//MoS_2/rGO	—	200	B	18	1.0	30	16.82	—	—	201
MG-1.6	GF//MG-1.6	—	500	B	60	1.2	60	19.4	—	—	202
Fe_3O_4/rGO	Fe_3O_4/rGO// Fe_3O_4/rGO	10 × 10	50[&]	S	—	1.5	120	4.3	—	—	203
rGO/Co_3O_4	rGO//rGO/Co_3O_4	7 × 7	250	B	—	1.6	30	18.63	2.88	—	204
rGO@$Na_4Ti_9O_{20}$ (rGO@NTO)	AC//rGO@NTO	\\	250	B	34	1.4	60	41.8	—	—	205
$Na_2Ti_3O_7$-CNT@rGO (NCNT@rGO)	*AC@rGO// NCNT@rGO	2.5 × 2.5	3000	B	50	±1.4 (145)[α]	35	129	3.6	—	206
$Na_{1.1}V_3O_{7.9}$@rGO (NVO@rGO)	Ag@rGO// NVO@rGO	—	2000	B	—	1.4	60	82.2	—	0.944	65
$NH_4V_4O_{10}$/rGO (NHVO/rGO)	*AC//NHVO/rGO	—	500	S	—	1.2	5	20.1	—	—	207
Silver-doped sepiolite intercalated graphene (AGS)	AGS//GS	11.5 × 5.5	600	B	10	1.2	175	20.7	—	0.871	208
PB/rGA	rGA//PB/rGA	—	2500	B	—	±1.4 (100)[α]	40	130	—	—	211
NiHCF/rGO	AC//NiHCF/rGO	6 × 6	500	B	—	0.6	30	22.8	\	0.6	212
$FePO_4$@rGO	AC//$FePO_4$@rGO	—	2337	B	200	±1.8 (100)[α]	~10	85.94	14.4	—	213
$FePO_4$@rGO	* AC// $FePO_4$@rGO	—	750	B	300	±1.4 (100)[α]	105	100	7.02[β]	—	214
NTP/rGO	*AC//NTP/rGO	2.8 × 2.8	1000	B	550	±1.4 (100)[α]	45	140	27 [β]	—	215
NTP/rPGO	AC//NTP/rPGO	4 × 6	786	B	20	1.4	10	32.25	18	—	216
N, S-NTP/rHGO	AC//N, S-NTP/ rHGO	4 × 6	800	B	20	1.4	~9	36.87	39.6	—	217
$Na_3V_2(PO_4)_3$/graphene	*AgCl/ graphene// $Na_3V_2(PO_4)_3$/ graphene	—	1000	B	100	±1.4 (100)[α]	~50	107.5	—	—	218

[a] Note: (1) * represent membrane CDI, [#] rate constant from fitting data through pseudo first-order adsorption, [α] the constant current mode (unit: mA g^{-1}), and [β] the maximum salt adsorption rate. (2) S and B indicate the single-pass and batch-mode CDI. (3) [γ] corresponds with an areal unit of mg m^{-2}.

efficiency 0.69 in 100 mg L^{-1} NaCl solution at 1.2 V.[148] Undoubtedly, superb CDI performance arising from structural excellence can also be achieved in a 3D block decorated with carbon nanoparticles, microporous carbon spheres, and graphene spheres.[111,149–152] In these 3D architectures, the ratio of guest carbon should be well-controlled in case of aggregation of graphene or guest carbon. Besides, Tai and coworkers' study showed that the pore structure and the layer thickness of guest carbon were essential for layered graphene/mesoporous carbon (G@MC) heterostructures.[153] In the one-pot Stober templating synthesis, the increase of the tetraethyl orthosilicate (TEOS) amount altered the mesopores from closed (C) to partially opened one (PO), and the rise of the graphene amount reduced the thickness of MC layers. Later, the thermal activation induced an open (O) mesoporous structure. After 120 min electro-adsorption at 1.5 V in 500 mg L^{-1} NaCl solution, thin MC layers with open mesopores (G@MC-O-thin) showed the highest value of 24.3 mg g^{-1}, compared to those of G@MC-PO-thin (22.2 mg g^{-1}), G@MC-PO-thick (17.1 mg g^{-1}), and G@MC-C-thick (11.8 mg g^{-1}) (Fig. 10E). Namely, the properties of guest carbon exhibited huge impacts on carbon/graphene composites. Similar phenomenon was observed in CNTs/graphene composites,[154–156] in which single-walled CNTs outperformed the multi-walled ones.[157]

Moreover, carbon networks serve as a skeleton to hold graphene sheets, where the homogeneously dispersed graphene sheets become the conducting agents to cement the segments. The effect of rGO in enhancing the electrical conductivity and structural integrity has been demonstrated in ACF webs prepared by electrospinning.[158] Qiu and coworkers suggested that 10 wt% rGO was the best ratio for attaining a high electrosorption capacity.[159] Wang and coworkers confirmed that the rGO embedding also affected the diameters and shapes of pores.[160] As a result, the binder-free rGO/ACF electrode with an optimally designed structure exhibited enhanced CDI property compared with ACF counterpart.[161] Likewise, rGO can be added to carbon aerogel (CA) to raise the electrochemical characteristics. High electrosorption capacities of 26.9 mg g^{-1} and 18.9 mg g^{-1} in NaCl solutions with concentrations of 500 mg L^{-1} and 250 mg L^{-1} were observed in the graphene-

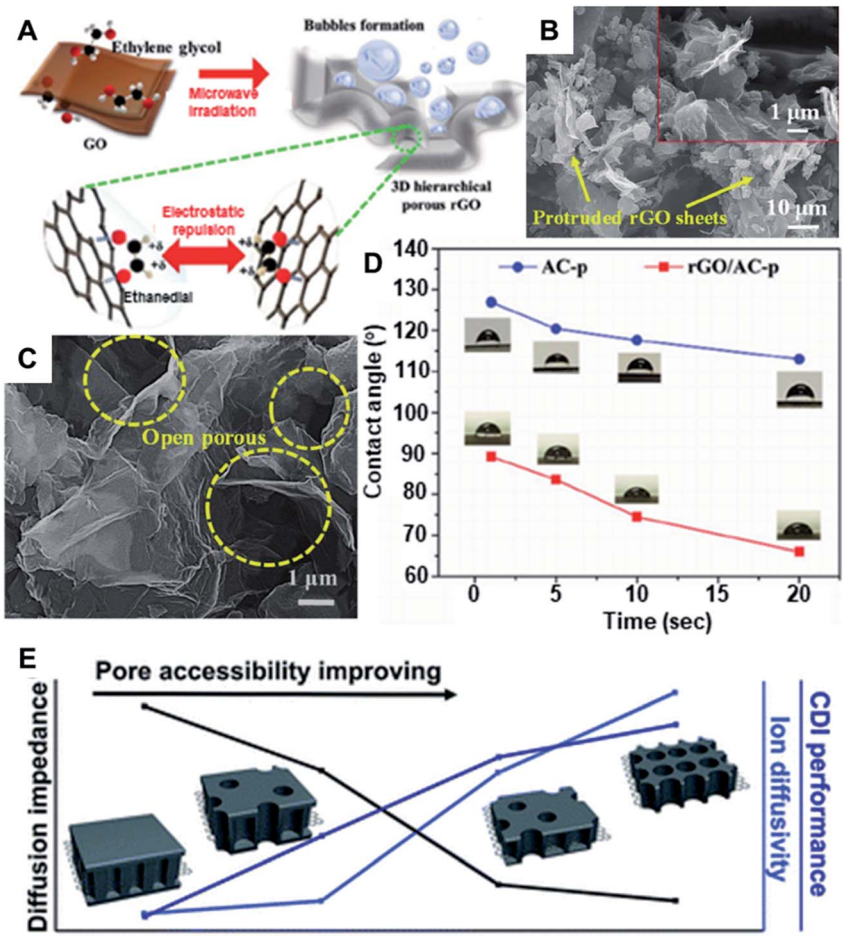

Fig. 10 (A) The proposed mechanism of the formation of 3D hierarchical porous structure of rGO/AC-p composite in the presence of EG under microwave irradiation. (B and C) SEM images showing wrinkled and protruded few-layer structure and open porous structure in the rGO/AC-p composite. (D) Optical micrographs of the water contact angle on the surface of electrodes as a function of contact time. Reproduced with permission from ref. 148. Copyright 2019 John Wiley and Sons. (E) The schematic demonstration of the pore accessibility control and its influences on ion diffusion and CDI performance. Reproduced with permission from ref. 153. Copyright 2018 The Royal Society of Chemistry.

composite CA.[162] When RGO-to-CA conducting network was integrated with ion-exchange membranes, an extremely high desalination efficiency of 98% was obtained.[163]

4.2 Pseudocapacitive material/graphene composite electrodes

Graphene composites with pseudocapacitive materials would achieve superb CDI performance with the synergistic ion storage in EDL and faradaic redox reaction. The pseudocapacitive storage of ions happens on the surface or near the surface of materials *via* either continuous changes in oxidation states or intercalation. Ideally, pseudocapacitive materials are able to accommodate 2.5 e^- per atom of accessible surface, overwhelming 0.17–0.2 e^- of carbon *via* EDLs.[164] This indicates the great application potential of pseudocapacitive materials for CDI. The most accepted pseudocapacitive materials, which must fit electrochemical marks in CV (broad peaks) and GCD (obscure platform) and quantitative kinetics identity ($b \approx 1$),[82] include conducting polymers, metal oxides and metal sulfides. These pseudocapacitive materials have been combined with graphene, leading to efficient composites. It is important to ensure fast charge transport to the composite surface, which requires the homogeneous dispersion of porous pseudocapacitive material on the graphene surface.

4.2.1 Polymer/graphene composite electrodes. Polymer involves in CDI by multifold roles. Polytetrafluoroethylene (PTFE) or polyvinylidene fluoride (PVDF) can serve as binders to integrate active materials and conductive carbon materials into electrode films. Also, pyrolysis of polymer is a prevalent source of carbon. rGO/resol like materials were carbonized at 900 °C under inert atmosphere, producing carbon/graphene composites.[165,166] Electrospun polymeric networks after carbonization acted as a platform to construct binder-free electrodes.[167] Besides, polymers can serve as electrode materials and ion-exchange membranes (IEMs) as some of them possess immense ion storage capability *via* surface redox reaction, and some transport certain ions.

As electrode materials, polypyrrole (PPy), polyvinyl alcohol (PVA), and polyaniline (PANI) are commonly used in graphene composites due to their high specific capacitance and good

chemical stability in nanoscale. Generally, the fabrication of a conductive polymer/graphene composite relies on the electrostatic assembly or co-deposition. The obtained graphene/PANI (G/PANI) nanocomposites displayed an intimate connection of PANI at the graphene edges with a large-scale π–π conjugation (Fig. 11A).[168] This structure ensured G/PANI to own large accessible surface area (394 $m^2 g^{-1}$) and facilitated charge transfer. As a result, G/PANI showed conductivity removal rates of 94% and 65% at 1.2 V in a MCDI device with initial conductivities of 500 and 1000 μS cm^{-1} (Fig. 11B and C), respectively. Moreover, introducing $SiW_{12}O_{40}^{4-}$ into PANI/exfoliated graphite carrier (SiW_{12}@PANI/EGC) enhanced the specific capacitance from 176 F g^{-1} to 352 F g^{-1} at 1 A g^{-1} in 1 M NaCl solution.[169] As electrodes of symmetrical CDI, SiW_{12}@-PANI/EGC reached 30 stable adsorption/desorption cycles with a SAC of 23.1 mg g^{-1} at 1.2 V in 500 mg L^{-1} NaCl solution. Except for variation in the synthesis, the test condition also has huge impacts on the polymer/graphene composites. As shown in the study of Xu *et al.*, the manipulation of CV sweeping at different potential windows could influence the doping level and polymeric conformation in GO/PPy.[170] When CV was scanned within the working window of 0 to −0.4 V (*vs.* SCE) in 1.0 M KCl, a gradual substituion of benzenesulfonate dopants with chloride ions was observed. While the potential was negatively shifted to −0.4 V–−1.0 V (*vs.* SCE), the deep reduction of GO/PPy induced irreversible polymeric conformational shrinks. Both of them inhibited ion storage. Besides, they proposed that the asymmetric CDI may be more effective in eliminating co-ion effects than symmetrical MCDI, especially in high salinity solution. Furthermore, PPy/GO composites showed excellent removal capacity of heavy metal ions in the orders of $Ag^+ < Cd^{2+} < Cu^{2+} < Pb^{2+} < Fe^{3+}$ (Fig. 11D).[171] PPy/GO composites owned a 2.67 times larger adsorption capacity of Cu^{2+} (41.51 mg g^{-1}) than PPy attributing to larger surface area (1325.4 $m^2 g^{-1}$), higher pore volume (4.10 $m^3 g^{-1}$), and lower charge transfer resistance (1.626 Ω cm^2). In addition to heavy metal ions, the GO/PPy on a copper-nickel foam (CNF) removed rhodamine B (RhB) with a capacity of 270.3 mg g^{-1} and a rate of 3.762 mg g^{-1} min^{-1}.[172] It also demonstrated that addition of salt ions helped the dissociation of dyes and accordingly the electrosorption capacity. However, it should be noted that superfluous salt ions would screen the electrostatic interaction between oppositely charged adsorbents and dyes.

In the context of IEMs in CDI, conductive polymer with high ion exchange capability and excellent electrical conductivity can benefit for electrochemical performance of graphene-based electrodes in many aspects. Casting cross-linked quaternized poly(vinyl alcohol) (C-qPVA) on a sponge-like N-doped rGO (NRGS) electrode drastically decreased the contact angles from 130 °C to 35 °C.[63] The quaternary ammonium groups on C-qPVA contributed to the enhanced hydrophilicity, reduced interfacial resistance, and facilitated anions transport. Subsequently, the as-fabricated A-NRGS electrode attained a high SAC of 11.30 mg g^{-1} in a MCDI system with a 250 mg L^{-1} NaCl feed at 1.2 V. Besides, rGO can tune the properties of an anion-exchange membrane (AEM). The addition of low-concentration GO in the mixture of PANI and PVDF could improve the PANI loading on PVDF matrix and the solvent-dispersion of PANI and PVDF as well as double the electrical conductivity. The obtained dense, hydrophilic, and conductive AEM can promote both the capacity and efficiency of ion adsorption.[173] In comparison, sulfonic group-containing graphene (SGO) through either ultrasonic-assisted or laser-induced assemblies allowed selective permeation of cations such as K^+, Na^+, Mg^{2+}, and Ca^{2+}.[174,175] As a result, the hybrid cation-exchange membranes of poly(-sodium 4-styrenesulfonate)/3,4-dihydroxy-L-phenylalanine/GO

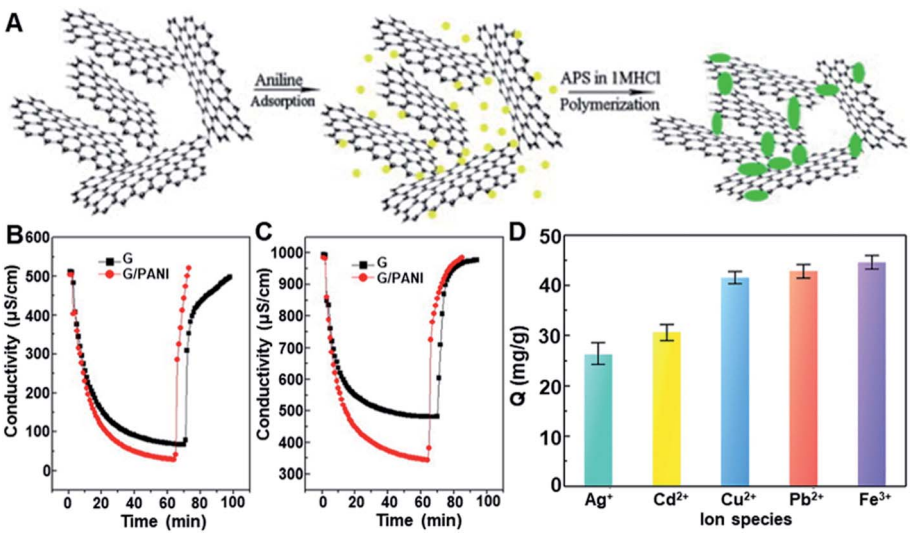

Fig. 11 (A) The *in situ* polymerization of PANI in the presence of graphene sheets. (B and C) Adsorption/desorption curves of graphene and G/PANI/G at 1.2 V in initial conductivities of 500 (B) and 1000 μS cm^{-1} (C). Reproduced with permission from ref. 168. Copyright 2014 Elsevier. (D) Adsorption of different ions by the PPy/GO composite electrode. Reproduced with permission from ref. 171. Copyright 2020 American Chemical Society.

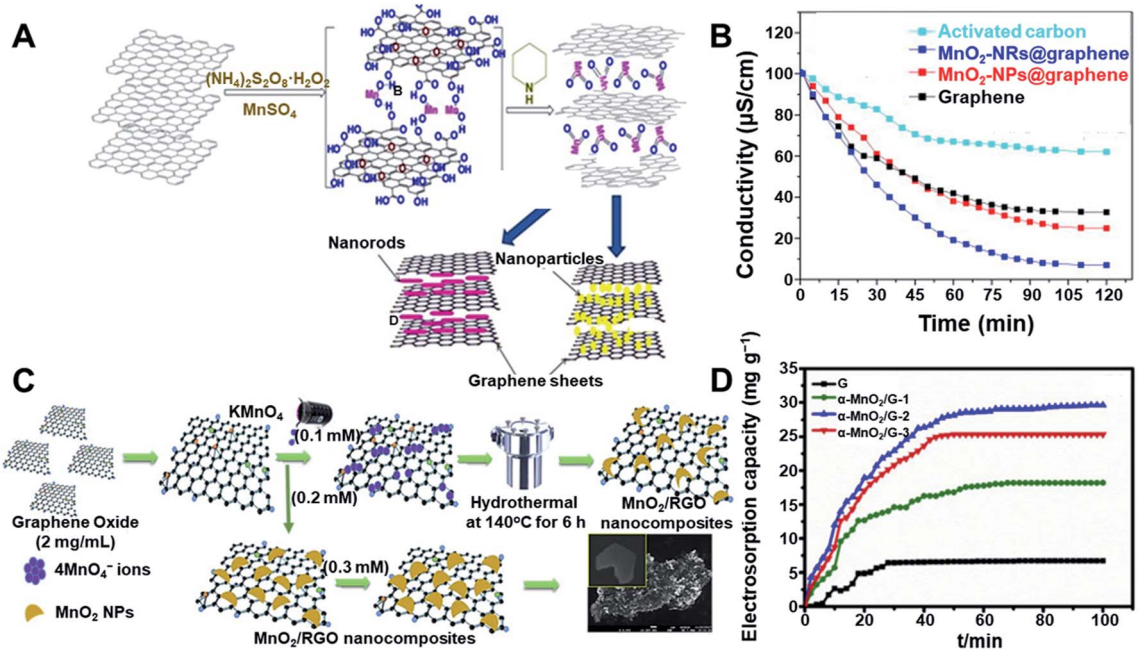

Fig. 12 (A) Schematic illustration for the one-pot synthesis procedure of MnO_2-nanostructures@graphene sheets as a sandwich structure. (B) CDI performance of the synthesized material electrode and AC in the NaCl solution at 1.2 V. Reproduced with permission from ref. 176. Copyright 2014 Elsevier. (C) Illustration of the nucleation growth mechanism of MnO_2/G-1, MnO_2/G-2, and MnO_2/G-3 nanocomposites. (D) Plots of electrosorption capacity *vs.* time for G, α-MnO_2/G-1, α-MnO_2/G-2, and α-MnO_2/G-3 electrodes in a 100 mg L^{-1} NaCl at 1.2 V. Reproduced with permission from ref. 184. Copyright 2020 Elsevier.

(PSS/L-DOPA/GO) and sulfonated poly(ether sulfone)-laser-induced graphene (SPES-LIG) displayed great potential for MCDI.

4.2.2 Metal oxide/graphene composites. Metal oxide/graphene composites can produce a favorable structure for ion storage as the metal oxides and graphene both act as reciprocal spacers, and graphene behaves like an electron highway. The synergistic effects allow ion storage *via* faradaic redox reaction in the near-surface of metal oxides and *via* electrostatic adsorption under the electric driving force at the solid–liquid interface of graphene. The graphene composites with mono-metal oxides such as MnO_2,[176] Mn_3O_4,[177] SnO_2,[178] Fe_2O_3,[179] TiO_2,[180] CeO_2,[181] ZrO_2,[182] and ZnO[183] generally display high SACs that are twice of the pristine graphene or even higher. Among the rest, manganese oxides with rich oxide states and a high theoretical specific capacitance up to 1400 F g^{-1} show the morphological dependent electrochemical performance. With the presence of $MnSO_4$, the MnO_2@graphene sandwich was prepared by a microwave exfoliation process, and the extended microwave subjecting time from 15 min to 30 min transformed the nanoparticles (NPs) to nanorods (NRs) (Fig. 12A).[176] MnO_2-NRs@graphene//MnO_2-NPs@graphene showed higher specific capacitance and desalination efficiency than graphene and AC (Fig. 12B). Besides, *via* oxidizing exterior carbon, MnO_4^- on the graphene matrix was spontaneously reduced to obtain uniformly dispersed prawn-like a-MnO_2/graphene (a-MnO_2/G) nanocomposite (Fig. 12C).[184] The rates of nucleation and subsequent growth of MnO_2 were associated with the concentration of $KMnO_4$ (0.1 M, 0.2 M, and 0.3 M). Given the limited faradaic ion storage in the sparse and small MnO_2 particles and inhibited ion transport in the denser and larger MnO_2 particles, the highest specific capacitance (375 F g^{-1}) was achieved in α-MnO_2/G-2 with a medium concentration of $KMnO_4$. The correspondingly SAC in a hybrid CDI with graphene anode and a-MnO_2/G-2 cathode was 29.5 mg g^{-1} at 1.2 V in 100 mg L^{-1} NaCl solution (Fig. 12D). Furthermore, dual functions of $KMnO_4$ in polymerization of pyrrole (Py) and formation of MnO_2 allowed the preparation of a 3D rGO-PPy-Mn composite.[185] At the mass ratio of 0.5 : 1 and 0.8 : 1 for Py/GO and $KMnO_4$/Py, the obtained RGO-$PPy_{0.5}$-$Mn_{0.4}$ showed three-times larger volume than its PPy-free counterpart and a higher surface area (331 m^2 g^{-1}) over rGO (120 m^2 g^{-1}) and PPy (63 m^2 g^{-1}). Both of them contributed to the overwhelming SAC of 18.4 mg g^{-1} at 2.0 V in a 1000 uS cm^{-1} NaCl solution. In brief, the introduction of metal oxides into the graphene matrix not only modifies the surface area, pore structure, and electrical conductivity, but also remarkably decreases the water contact angle.[186–189] Normally, a more hydrophilic surface attained at the optimal ratio of metal oxide/graphene causes a prominent increase in electrosorption capacity and rate.[190,191] Impressively, hybrid CDI with a graphene anode and a metal oxide/graphene cathode,[192] or in a rationally-designed composite with target chemisorption[193] manifests the desired ion selectivity.

Since two metal atoms provide more sites for faradaic charge transfer, double metal oxide (DMO)/graphene composites draw great attention in CDI as well. With rGO as the electron highway and co-crystallization platform, submicron-scale and uniformly-distributed $MnFe_2O_4$ particles were obtained on the

surface of rGO.[194] The rational layout of $MnFe_2O_4$ and porous rGO facilitated the deionization, showing a capacitance of 237 F g^{-1} in a three-electrode measurement and a SAC of 8.9 mg g^{-1} and 100% regeneration of multiple cycles in a hybrid CDI with a $MnFe_2O_4$/porous rGO electrode and a rGO electrode. As the spinel compounds, $MnFe_2O_4$ (MFO)/rGO was demonstrated to be superior to MnO_2/rGO. In a HCDI, the MFO-rGO//rGO electrode pair showed SAC of 29.44 mg g^{-1} and ASAR of 22.07 μg g^{-1} s^{-1}. In comparison, the SAC and ASAR for the MnO_2-rGO//rGO electrode pair were 21.16 mg g^{-1} and 14.39 μg g^{-1} s^{-1}. With the synergistic pseudocapacitive-EDL effects, the MFO-rGO//MnO_2-rGO attained the highest SAC of 38.28 mg g^{-1} with the second fastest ASAR of 20.8 μg g^{-1} s^{-1}.[195] Likewise, vertically-aligned CuAl-layered double oxides grown on rGO (CuAl-LDO/rGO) also showed super CDI performance with a SAC of 64.0 mg g^{-1} at 1.2 V in 1000 mg L^{-1} NaCl solution.[196] Besides, DMOs converted from layered double hydroxides (LDHs) showed unique microporous structure due to the release of gases. As expected, MgAl-Ox/G showed larger SSA than MgAl-LDHs/GO (137 m^2 g^{-1} *vs.* 31 m^2 g^{-1}). Assembly of MgAl-Ox/G anode and nitric acid-treated AC cathode in a single-pass HCDI yielded a SAC of 13.6 mg g^{-1} with charge efficiency of 88.7% toward 500 mg L^{-1} NaCl solution, which was obviously higher than those of MgAl-Ox//AC and MgAl-Ox/G//AC.[197] The outstanding SAC maintained to be 13 mg g^{-1} after 12 desalination/regeneration cycles. Moreover, the selective adsorption of ions was achieved in NiCoAl-LMO/rGO composites with the sequence of F^- > Cl^- > Br^- > NO_3^- > SO_4^{2-}.[198] When the potential of 1.4 V was applied, the SAC for 500 mg L^{-1} NaF solution reached 24.5 mg g^{-1}. It was found that the Co atoms played a pivotal role in the defluorination as the ratio of Co^{3+}/Co^{2+} in positively charged NiCoAl-LMO/rGO varied from 0.75 to 1.6 during the charging process.

4.2.3 MoS_2/graphene composite. Molybdenum disulfide (MoS_2) is analogous to graphene, showing a layered structure bound with van der Waals force and suffering easy agglomeration at exfoliated states. In contrast to graphene with ions stored in EDL, MoS_2 delivers different ion storage features. The interlayer spacing of MoS_2 (6.20 Å) is wide enough to accommodate reversible intercalation/de-intercalation of sodium ions (diameter: 1.02 Å),[199] but the poor conductivity and insufficient material utilization in bulk MoS_2 drag the storage ability. In this regard, MoS_2/graphene composites, which completely exploit the surface-confined effect and high conductivity of graphene, are supposed to attain a desirable structure for superior CDI performance. In the one-step hydrothermal reaction, the composition of solvents influences the morphology of obtained MoS_2/rGO. At the volume ratio of water and ethanol of 2 : 1, MoS_2 displayed a 3D flower-like architecture entangled with the corrugated and scrolled rGO sheets (MSG-1) (Fig. 13A).[200] As the volume ratio increased to 3 : 2, MoS_2 attained a nanoflake architecture attached to the surface of rGO sheets (MSG-2) (Fig. 13B). In a HCDI with an AC anode, MSG-1 as a cathode outperformed MSG-2, achieving a high SAC of 16.82 mg g^{-1} at

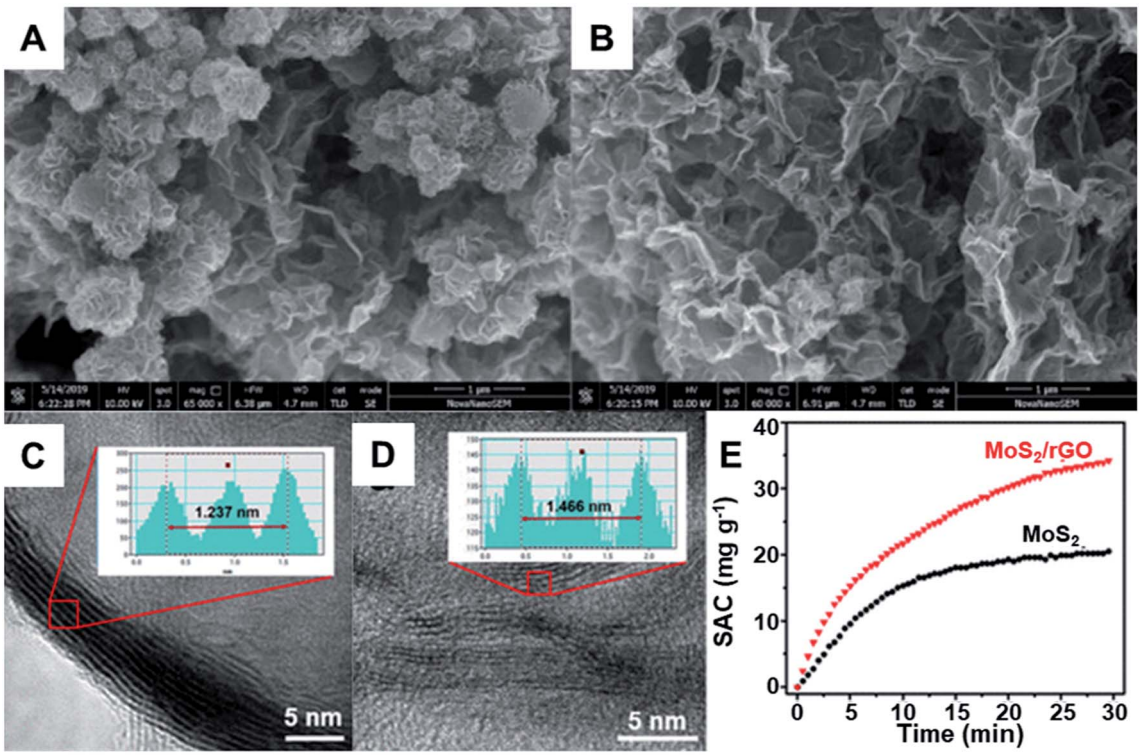

Fig. 13 (A and B) SEM images of MSG-1 (A) and MSG-2 (B). Reproduced with permission from ref. 200. Copyright 2020 Elsevier. (C and D) TEM images of MoS_2 (C) and MoS_2/rGO (D). (E) Plots of SAC *vs.* desalination time in 300 mg L^{-1} NaCl solution at 1.4 V with a flow rate of 12 mL min^{-1}. Reproduced with permission from ref. 202. Copyright 2020 American Chemical Society.

1.0 V in 200 mg L^{-1} NaCl solution, because MSG-1 held larger SSA and lower charge transport resistance. In addition, the ratio of graphene could tune the nucleation and growth rates of MoS_2. Small loading amount of graphene inclined to produce thick and stacked MoS_2 sheets, whereas overdosed graphene led to the formation of aggregated graphene and MoS_2 of smaller dimensions.[201] The favorable CDI performance was achieved at the graphene ratio of 1.6 wt% with thin-sheet-like MoS_2 well dispersed on the graphene surface (MG-1.6). The HCDI with an AC anode and a MG-1.6 cathode delivered high SACs of 14.3 mg cm^{-3} and 19.4 mg g^{-1} in 500 mg L^{-1} NaCl solution. This HCDI could also effectively remove Cu^{2+} and Pb^{2+}. What is more, the incorporation of rGO in the composite induced the expansion of interlayer spacing in MoS_2 from 0.62 to 0.73 nm (Fig. 13C and D).[202] It brought about more sites and larger space accessible for cation storage and decreased resistance for cation diffusion. Such a MoS_2/rGO composite in a HCDI device attained a remarkable SAC of 34.20 mg g^{-1} and a charge efficiency of 97% in 300 mg L^{-1} NaCl aqueous solution (Fig. 13E).

4.3 Battery material/graphene composite electrodes

Desalination battery or battery-type CDI was first proposed in 2012 with an Ag/AgCl anode for chloride capture and a $Na_{2-x}Mn_5O_{10}$ (NMO) cathode for sodium insertion (note: the classification of cathode and anode is based on the electrolysis cell).[51] The success of this architecture and its limited sodium ion storage in NMO (35 mA h g^{-1}) drew more attention to readily available battery materials. With ion storage at crystallographic sites or between the atomic planes, battery materials, like sodium-containing metal oxides, Prussian blue, and metal phosphates, can combine with graphene to show intriguing CDI performance when hybrid electrodes and hybrid CDI cells are synergistically adopted.

4.3.1 Sodium-containing metal oxide/graphene composite. For sodium-containing metal oxides storing ions with bulk intercalation, the theoretical capacity that suggests the maximized sites for accommodating cations (Li^+, Na^+, and K^+) should be considered carefully, in addition to morphology, pore structure, hydrophilic surface, metal oxide/graphene ratio, and electrical conductivity. Typical anode materials of batteries, like Co_3O_4 and Fe_3O_4, delivered a theoretical capacity up to 1000 mA h g^{-1} *vs.* Li^+. Toward CDI, the SAC of Fe_3O_4/rGO nanocomposite reached 4.3 mg g^{-1} at 1.5 V in the feeding water containing 28.8 mg L^{-1} of $CaCl_2$, 22.0 mg L^{-1} of $MgSO_4 \cdot 7H_2O$, and 39.0 mg L^{-1} of $NaHCO_3$,[203] and rGO/Co_3O_4 achieved SAC of 18.63 mg g^{-1} at 1.6 V for 250 mg L^{-1} NaCl aqueous solution.[204] Cathode materials such as $Na_xTi_yO_x$, $Na_xV_yO_z$, and $Na_xMn_yO_z$ with theoretical capacities of 100–250 mA h g^{-1} *vs.* Li^+ have demonstrated their success in Na^+ intercalation chemistry.[53,205,206] In a HCDI, $Na_4Ti_9O_{20}$ (NTO) cathode coupled with AC anode delivered a SAC of 23.35 mg g^{-1} (1.4 V and 250 ppm NaCl solution).[205] This SAC could be further improved to 41.8 mg g^{-1} in AC//rGO@NTO HCDI as the introduction of graphene enhanced the conductivity of NTO (Fig. 14A). The charge efficiency for AC/rGO@NTO HCDI approached to 1, which suggested high ion selectivity of rGO/NTO electrodes and the negligible impaction of co-ion repulsion. Likewise, membrane-HCDI comprising the AC@rGO film (anode) and a binder-free $Na_2Ti_3O_7$-CNT@rGO (NCNT@rGO) film (cathode) attained high electrosorption capacity (129 mg g^{-1}), desalination rate (0.037 mg g^{-1} s^{-1}), and charge efficiency (>90%) under constant current mode in 3000 mg L^{-1} NaCl solution.[206] More importantly, AC@rGO//NCNT@rGO consumed less energy and attained higher energy recovery than AC//rGO (0.39 W h g^{-1} and 23% *vs.* 0.64 W h g^{-1} and 14%) (Fig. 14B). Besides, coupling ribbon-like $Na_{1.1}V_3O_{7.9}$@rGO (NVO@rGO) electrode for sodium ion intercalation with Ag@rGO electrode for chloride ion intercalation can develop a dual-ion hybrid CDI (Di-HCDI) system.[65] Remarkable SAC of 82.2 mg g^{-1} and charge efficiency of 94.4% were achieved at 1.4 V with feeding water of 2000 mg L^{-1} NaCl solution. Shortly, hybrid metal oxide/graphene electrodes offer intriguing efficiency for ion removal and charge utilization benefiting from ion selectivity and bulk intercalation mechanism of battery materials, and conductivity

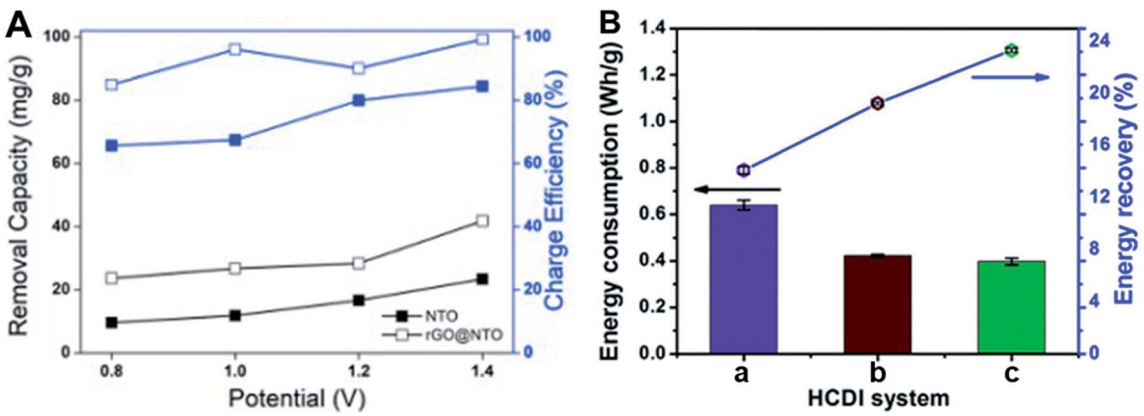

Fig. 14 (A) Comparison on removal capacity and charge efficiency between NTO and rGO@NTO. Reproduced with permission from ref. 205. Copyright 2018 Elsevier. (B) The energy consumption and energy recovery of NCNT//AC composite (a), NCNT@rGO-2//AC@rGO-2 (b) and NCNT@rGO-1//AC@rGO-1 (c) systems at an applied current of 1 mA, ~3000 mg L^{-1} NaCl solution. Reproduced with permission from ref. 206. Copyright 2019 The Royal Society of Chemistry.

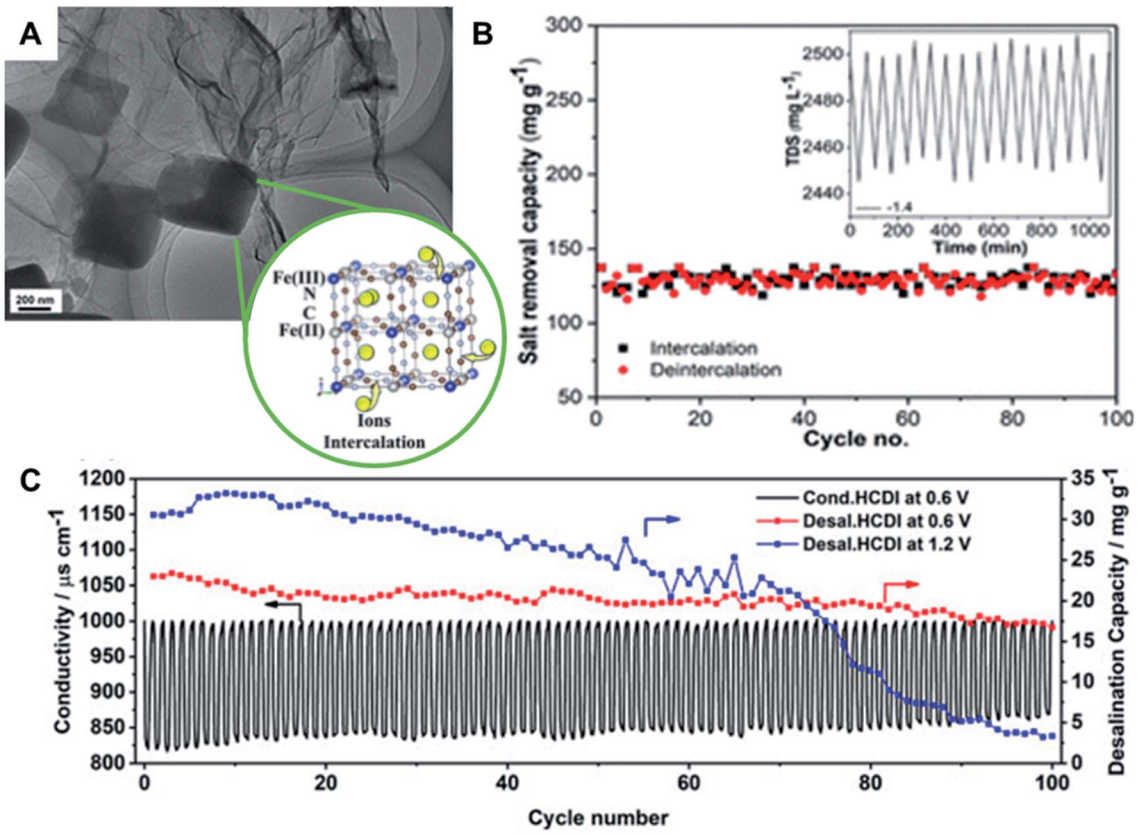

Fig. 15 (A) TEM Image of PB/rGA (inset: schematic crystal structure of Prussian blue after Na^+ intercalation during charging process). (B) Cycle performance for voltage ranges of 1.4 to −1.4 V. Reproduced with permission from ref. 211. Copyright 2019 American Chemical Society. (C) Desalination-regeneration experiment at 0.6 V and 1.2 V for 100 cycles. Reproduced with permission from ref. 212. Copyright 2019 Elsevier.

and surface-confined effects of graphene materials.[207] These advantages would be amplified in a HCDI when an anionic intercalation electrode is applied.[208] The sizes of adsorbed ions also substantially affect the SAC. For example, $LiNi_{0.6}Co_{0.2}Mn_{0.2}O_2$ exhibited abundant adsorption of Li^+, but negligible capabilities for the adsorption of Na^+, K^+, Mg^{2+}, and Cu^{2+}.[209]

4.3.2 Prussian blue/graphene composite. Prussian blue (PB) and its analog (PBA) are emerging sodium intercalation materials with a general formula of $A_xM_y^A[M^B(CN)_6]_z \cdot nH_2O$ (A: Li, Na, or K; M^A and M^B: Mn, Fe, Co, Ni, Cu, or Zn).[210] Since M^A and M^B alternatively locate on the corners of an octahedron and are connected by the conjugated cyanide ions, PB and PBA hold an open-framework structure with large interstitial voids, allowing strain-free accommodation of mostly alkaline metal cations. However, the great desalination potentials of PB and PBA are seriously restricted by their poor electrical conductivity, which could be significantly alleviated by the presence of graphene. As expected, the embedding of PB nanocubes into rGO aerogel (PB/rGA) promoted the SAC to 130 mg g^{-1} at the current density of 100 mA g^{-1} in the potential range of 0–1.4 V when rGA was exploited as anode, and mass ratio for cathode and anode was 2 : 1.[211] The energy consumption was as low as 0.23 W h g^{-1} at a desorption voltage of −0.2 V, and the energy recovery reached 39% at 0 V. The excellent desalination performance was attributed to the easy capture of Na^+ in the cage structure of PB. The strain-free and reversible insertion/extraction of Na^+ endowed PB/rGO to show stable adsorption/desorption behavior for at least 100 cycles (Fig. 15A and B). More prominently, HCDI equipped with AC anode and nickel hexacyanoferrate/rGO (NiHCF/rGO) cathode achieved a high SAC of 22.8 mg g^{-1} at an extremely low potential of 0.6 V, which was almost five times larger than that in AC//AC CDI.[212] The HCDI operated at 0.6 V performed stably with a capacity retention of 76% for 100 cycles, overwhelming HCDI at 1.2 V (Fig. 15C).

4.3.3 Metal phosphate/graphene composite. Structurally stable and diverse phosphates have also shown prominent Na^+ intercalation chemistry. $FePO_4$ nanosphere, which possesses a high theoretical capacity of 175 mA h g^{-1} in sodium-ion batteries, displayed a SAC of 50.13 mg g^{-1} and a desalination rate of 0.079 mg g^{-1} s^{-1} at 1.8 V in batch-mode HCDI with 30 mL NaCl solution of 40 mmol L^{-1}.[213] With the introduction of graphene, the obtained $FePO_4$@rGO exhibited an enhanced desalination capacity of 85.49 mg g^{-1} and the rate of 0.24 mg g^{-1} s^{-1} due to the mesoporous structure and graphene covering. Meanwhile, the decrease in energy consumption (9.0×10^{-4} kW h) and total cost in removing a gram of NaCl in one cycle (¥ 6.2) allowed HCDI to show great potential for application in large-scale desalination. A similar $FePO_4$@rGO was applied in MHCDI (AC anode) as well, delivering a SAC of

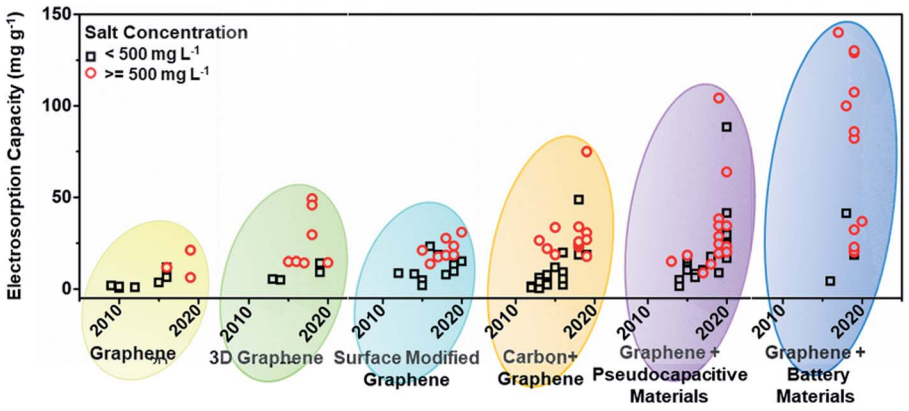

Fig. 16 The explosive increase of electrosorption capacity for graphene-based electrodes toward CDI from 2009 to September 2020.

100 mg g^{-1} under the constant current adsorption (100 mA g^{-1}).[214] Likewise, the adoption of graphene as a crystallization platform and conductivity enhancer could promote the CDI performance of $NaTi_2(PO_4)_3$ (NTP).[215] Under constant current of 100 mA g^{-1}, MCDI comprising AC//NTP/rGO afforded a SAC of 140 mg g^{-1} in the 1st cycle that retained 100 mg g^{-1} after 100th cycles. As the current density increased to 1000 mA g^{-1}, an extraordinarily rapid desalination rate (0.45 mg g^{-1} s^{-1}) was observed, which corresponded to a drop of SAC to 27 mg g^{-1}. Alternatively, under the constant potential of 1.4 V, NTP/reduced porous GO (NTP/rPGO) composites yielded a SAC of 33.25 mg g^{-1} and a desalination rate of 0.30 mg g^{-1} s^{-1} (conductivity of NaCl solution: 1600 μS cm^{-1}),[216] while nitrogen and sulfur co-doped NTP/hole graphene (N, S-NTP/rHGO) delivered a desalination of 36.87 mg g^{-1} and a rapid ion removal rate of 0.66 mg g^{-1} s^{-1} (initial NaCl concentration: 800 mg L^{-1}).[217] Besides, a $Na_3V_2(PO_4)_3$/graphene hybrid aerogel could serve as the sodium electrode combined with a AgCl/graphene hybrid aerogel electrode (as the chloride electrode) in a CDI cell.[218] The assembled Di-HCDI exhibited the SAC as high as 107.5 mg g^{-1} after 50 cycles at the current density of 100 mA g^{-1}. As discussed above, the advances of single-phosphate electrodes in CDI would promote the exploration of other phosphate framework materials, like pyrophosphates and mixed-phosphates.[219]

5. Conclusion and outlook

Graphene and its composites are the most promising alternative to activated carbon with an expectation to achieve highly efficient, cost-effective, and environment-friendly capacitive deionization. The intrinsic nature of the high theoretical surface area and electrical conductivity endows graphene with superb conditions for electrostatic ion adsorption. Structurally engineered graphene in terms of 3D porous graphene integrates the in-plane and out-of-plane pores and hydrophilic surface, allowing the promotion of desalination capacity and rate. Besides, graphene composites with either pseudocapacitive materials or battery materials, which take the advantages of surface-confined effects and high conductivity in graphene, maximize synergistic adsorption capability of electric double layers and faradaic redox reaction and promote the ion selectivity. The basic design principle is to provide salt ions with quick access to the surface of graphene-based electrodes. The rational selection of anode and cathode materials can alleviate the co-ion repulsion effects and elevate the selectivity up to the level comparable to cation/anion-exchange-membrane-coupled electrodes. With the evolution of test configurations from symmetrical to asymmetrical and finally to hybrid ones, recent progress of CDI takes in-depth understanding of ion adsorption, selectivity, and reversibility.

In the recent decade, the ion adsorption capacity of graphene-based electrodes has experienced an explosive growth from 1.85 mg g^{-1} to ~150 mg g^{-1} (Fig. 16). Meanwhile, the charge efficiency approximately approaches to the ideal value of 1. However, the lack of standard evolution criteria lowers the significance in comparing electrode materials with absolute values. Reliable comparison should be conducted within the same CDI system. Besides, lab-scale CDI measurement, to great extent, relies on the small electrode dimensions (3 × 3 cm^2 or 5 × 5 cm^2), the relatively thin electrode film, batch-mode water recycling, and constant current test, most of which are not applicable or practical in large-scale desalination. Reducing the gaps between laboratory and industrial evaluation is urgent and of great importance for the future development of CDI. In addition, most CDI cells claim their outstanding adsorption/desorption stability within 5–100 cycles, which is far below the requirements for practical application.

Besides, CDI has extended their success in ion adsorption from alkaline metal ions (*e.g.*, Li^+, Na^+, and K^+) to heavy metal ions (*e.g.*, U(VI) ions, Pb^{2+}, Hg^+, *etc.*) and organic micro-pollutants (*e.g.*, dyes). CDI has application potential for disinfection of drinking water as well. In most cases, the chemically engineered graphene electrodes are more efficient than the pristine one. But when the multiple ions with same symbols exist, the sole adsorption of a specific ion is still a great challenge.

Conflicts of interest

There are no conflicts to declare.

Acknowledgements

We are grateful for support from the National Science Foundation (CMMI-1661699).

References

1 M. A. Shannon, P. W. Bohn, M. Elimelech, J. G. Georgiadis, B. J. Marinas and A. M. Mayes, *Nature*, 2008, **452**, 301–310.
2 M. Elimelech and W. A. Phillip, *Science*, 2011, **333**, 712–717.
3 S. H. Lin, *Environ. Sci. Technol.*, 2020, **54**, 76–84.
4 F. A. AlMarzooqi, A. A. Al Ghaferi, I. Saadat and N. Hilal, *Desalination*, 2014, **342**, 3–15.
5 J. Choi, P. Dorji, H. K. Shon and S. Hong, *Desalination*, 2019, **449**, 118–130.
6 H. Wang, T. T. Yan, J. J. Shen, J. P. Zhang, L. Y. Shi and D. S. Zhang, *Environ. Sci.: Nano*, 2020, **7**, 317–326.
7 G. Z. Wang, T. T. Yan, J. P. Zhang, L. Y. Shi and D. S. Zhang, *Environ. Sci. Technol.*, 2020, **54**, 8411–8419.
8 L. Chang and Y. H. Hu, *RSC Adv.*, 2016, **6**, 47285–47291.
9 A. Thamilselvan, A. S. Nesaraj and M. Noel, *Int. J. Environ. Sci. Technol.*, 2016, **13**, 2961–2976.
10 M. H. Qin, A. Deshmukh, R. Epsztein, S. K. Patel, O. M. Owoseni, W. S. Walker and M. Elimelech, *Desalination*, 2019, **455**, 100–114.
11 S. K. Patel, M. Qin, W. S. Walker and M. Ehmelech, *Environ. Sci. Technol.*, 2020, **54**, 3663–3677.
12 L. Wang, J. E. Dykstra and S. H. Lin, *Environ. Sci. Technol.*, 2019, **53**, 3366–3378.
13 P. Liang, Z. J. Ren and X. Huang, *Environ. Sci.: Water Res. Technol.*, 2020, **6**, 241–242.
14 X. Liu, S. Shanbhag, T. V. Bartholomew, J. F. Whitacre and M. S. Mauter, *ACS ES&T Engg*, 2020, DOI: 10.1021/acsestengg.1020c00094.
15 J. E. Dykstra, S. Porada, A. van der Wal and P. M. Biesheuvel, *Water Res.*, 2018, **143**, 367–375.
16 S. Porada, L. Zhang and J. E. Dykstra, *Desalination*, 2020, **488**, 114383.
17 Z. Sun, S. Fang and Y. H. Hu, *Chem. Rev.*, 2020, **120**, 10336–10453.
18 H. Wang, K. Sun, F. Tao, D. J. Stacchiola and Y. H. Hu, *Angew. Chem., Int. Ed.*, 2013, **52**, 9210–9214.
19 W. Wei, K. Sun and Y. H. Hu, *J. Mater. Chem. A*, 2016, **4**, 12054–12057.
20 W. Wei, B. Y. Hu, F. M. Jin, Z. Z. Jing, Y. X. Li, A. A. G. Blanco, D. J. Stacchiola and Y. H. Hu, *J. Mater. Chem. A*, 2017, **5**, 7749–7752.
21 L. T. Qu, Y. Liu, J. B. Baek and L. M. Dai, *ACS Nano*, 2010, **4**, 1321–1326.
22 J. Qi, N. Benipal, H. Wang, D. J. Chadderdon, Y. B. Jiang, W. Wei, Y. H. Hu and W. Z. Li, *ChemSusChem*, 2015, **8**, 1147–1150.
23 J. S. Zhou, H. H. Song, L. L. Ma and X. H. Chen, *RSC Adv.*, 2011, **1**, 782–791.
24 K. Smith, R. Parrish, W. Wei, Y. Z. Liu, T. Li, Y. H. Hu and H. Xiong, *ChemSusChem*, 2016, **9**, 1397–1402.
25 L. Wang, J. Deng, J. T. Deng, Y. H. Fei, Y. Fang and Y. H. Hu, *J. Mater. Chem. A*, 2020, **8**, 13385–13392.
26 L. Chang, W. Wei, K. Sun and Y. H. Hu, *J. Mater. Chem. A*, 2015, **3**, 10183–10187.
27 L. Chang, D. J. Stacchiola and Y. H. Hu, *ACS Appl. Mater. Interfaces*, 2017, **9**, 24655–24661.
28 L. Chang, D. J. Stacchiola and Y. H. Hu, *J. Mater. Chem. A*, 2017, **5**, 23252–23258.
29 L. Chang, D. J. Stacchiola and Y. H. Hu, *Ind. Eng. Chem. Res.*, 2018, **57**, 3610–3616.
30 L. Chang, K. Sun and Y. H. Hu, *ACS Appl. Mater. Interfaces*, 2018, **10**, 33162–33169.
31 L. Chang and Y. H. Hu, *Matter*, 2019, **1**, 596–620.
32 L. H. Zheng, H. R. Su, J. Z. Zhang, L. S. Walekar, H. V. Molamahmood, B. X. Zhou, M. C. Long and Y. H. Hu, *Appl. Catal., B*, 2018, **239**, 475–484.
33 H. B. Li, T. Lu, L. K. Pan, Y. P. Zhang and Z. Sun, *J. Mater. Chem.*, 2009, **19**, 6773–6779.
34 R. K. Upadhyay, N. Soin and S. S. Roy, *RSC Adv.*, 2014, **4**, 3823–3851.
35 A. Aghigh, V. Alizadeh, H. Y. Wong, M. S. Islam, N. Amin and M. Zaman, *Desalination*, 2015, **365**, 389–397.
36 J. Li, B. X. Ji, R. Jiang, P. P. Zhang, N. Chen, G. F. Zhang and L. T. Qu, *Carbon*, 2018, **129**, 95–103.
37 J. W. Blair and G. W. Murphy, *Adv. Chem. Ser.*, 1960, **27**, 206–223.
38 J. C. Farmer, D. V. Fix, G. V. Mack, R. W. Pekala and J. F. Poco, *J. Electrochem. Soc.*, 1996, **143**, 159–169.
39 K. Dai, L. Y. Shi, J. H. Fang, D. S. Zhang and B. K. Yu, *Mater. Lett.*, 2005, **59**, 1989–1992.
40 L. D. Zou, L. X. Li, H. H. Song and G. Morris, *Water Res.*, 2008, **42**, 2340–2348.
41 G. W. Reid, *Field operation of a 20 gallons per day pilot plant unit for electrochemical desalination of brackish water*, U.S. Dept. of the Interior, 1968.
42 A. M. Johnson and J. Newman, *J. Electrochem. Soc.*, 1971, **118**, 510–517.
43 J. C. Farmer, D. V. Fix, G. V. Mack, R. W. Pekala and J. F. Poco, *J. Electrochem. Soc.*, 1996, **143**, 159–169.
44 R. Zhao, P. M. Biesheuvel and A. van der Wal, *Energy Environ. Sci.*, 2012, **5**, 9520–9527.
45 M. Andelman, *J. Mater. Sci. Chem. Eng.*, 2014, **2**, 16–22.
46 J. B. Lee, K. K. Park, H. M. Eum and C. W. Lee, *Desalination*, 2006, **196**, 125–134.
47 H. B. Li, Y. Gao, L. K. Pan, Y. P. Zhang, Y. W. Chen and Z. Sun, *Water Res.*, 2008, **42**, 4923–4928.
48 Y. J. Kim and J. H. Choi, *Sep. Purif. Technol.*, 2010, **71**, 70–75.
49 Z. L. Chen, H. T. Zhang, C. Yang, X. W. Sun, H. F. Guo, C. X. Wu, F. Q. Xue and L. Gao, *Desalin. Water Treat.*, 2013, **51**, 3489–3496.
50 E. Bayram and E. Ayranci, *Electrochim. Acta*, 2011, **56**, 2184–2189.
51 M. Pasta, C. D. Wessells, Y. Cui and F. La Mantia, *Nano Lett.*, 2012, **12**, 839–843.
52 P. Y. Liu, T. T. Yan, L. Y. Shi, H. S. Park, X. C. Chen, Z. G. Zhao and D. S. Zhang, *J. Mater. Chem. A*, 2017, **5**, 13907–13943.

53 J. Lee, S. Kim, C. Kim and J. Yoon, *Energy Environ. Sci.*, 2014, **7**, 3683–3689.
54 X. Gao, A. Omosebi, J. Landon and K. L. Liu, *Energy Environ. Sci.*, 2015, **8**, 897–909.
55 C. J. Gabelich, T. D. Tran and I. H. Suffet, *Environ. Sci. Technol.*, 2002, **36**, 3010–3019.
56 M. W. Ryoo, J. H. Kim and G. Seo, *J. Colloid Interface Sci.*, 2003, **264**, 414–419.
57 C. M. Yang, W. H. Choi, B. K. Na, B. W. Cho and W. I. Cho, *Desalination*, 2005, **174**, 125–133.
58 S. I. Jeon, J. G. Yeo, S. Yang, J. Choi and D. K. Kim, *J. Mater. Chem. A*, 2014, **2**, 6378–6383.
59 K. B. Hatzell, E. Iwama, A. Ferris, B. Daffos, K. Urita, T. Tzedakis, F. Chauvet, P. L. Taberna, Y. Gogotsi and P. Simon, *Electrochem. Commun.*, 2014, **43**, 18–21.
60 T. J. Petek, N. C. Hoyt, R. F. Savinell and J. S. Wainright, *J. Electrochem. Soc.*, 2016, **163**, 5001–5009.
61 L. Chang and Y. H. Hu, *J. Phys. Chem. Solids*, 2018, **116**, 347–352.
62 S. Porada, R. Zhao, A. van der Wal, V. Presser and P. M. Biesheuvel, *Prog. Mater. Sci.*, 2013, **58**, 1388–1442.
63 X. Y. Gu, Y. H. Deng and C. Y. Wang, *ACS Sustainable Chem. Eng.*, 2017, **5**, 325–333.
64 J. Ma, L. Wang and F. Yu, *Electrochim. Acta*, 2018, **263**, 40–46.
65 Z. S. Yue, Y. L. Ma, J. W. Zhang and H. Li, *J. Mater. Chem. A*, 2019, **7**, 16892–16901.
66 J. H. Lee, W. S. Bae and J. H. Choi, *Desalination*, 2010, **258**, 159–163.
67 X. P. Quan, Z. B. Fu, L. Yuan, M. L. Zhong, R. Mi, X. Yang, Y. Yi and C. Y. Wang, *RSC Adv.*, 2017, **7**, 35875–35882.
68 J. P. L. Lazarte, L. Bautista-Patacsil, R. C. P. Eusebio, A. H. Orbecido and R. A. Doong, *Nanomaterials*, 2019, **9**, 1319.
69 Z. L. Chen, C. Y. Song, X. W. Sun, H. F. Guo and G. D. Zhu, *Desalination*, 2011, **267**, 239–243.
70 L. Wang, M. Wang, Z. H. Huang, T. X. Cui, X. C. Gui, F. Y. Kang, K. L. Wang and D. H. Wu, *J. Mater. Chem.*, 2011, **21**, 18295–18299.
71 C. A. R. Perez, O. N. Demirer, R. L. Clifton, R. M. Naylor and C. H. Hidrovo, *J. Electrochem. Soc.*, 2013, **160**, E13–E21.
72 F. Al Suwaidi, H. Younes, V. Sreepal, R. R. Nair, C. Aubry and L. Zou, *2D Mater.*, 2019, **6**, 045010.
73 M. R. Vengatesan, I. F. F. Darawsheh, B. Govindan, E. Alhseinat and F. Banat, *Electrochim. Acta*, 2019, **297**, 1052–1062.
74 H. B. Li, L. K. Pan, T. Lu, Y. K. Zhan, C. Y. Nie and Z. Sun, *J. Electroanal. Chem.*, 2011, **653**, 40–44.
75 W. H. Shi, C. Z. Ye, X. L. Xu, X. Y. Liu, M. Ding, W. X. Liu, X. H. Cao, J. N. Shen, H. Y. Yang and C. J. Gao, *ACS Omega*, 2018, **3**, 8506–8513.
76 P. Ratajczak, M. E. Suss, F. Kaasik and F. Beguin, *Energy Storage Mater.*, 2019, **16**, 126–145.
77 J. Oladunni, J. H. Zain, A. Hai, F. Banat, G. Bharath and E. Alhseinat, *Sep. Purif. Technol.*, 2018, **207**, 291–320.
78 H. Helmholtz, *Ann. Phys. Chem.*, 1853, **165**, 23.
79 B. E. Conway, *Electrochemical Supercapacitors Scientific Fundamentals and Technological Applications*, Kluwer Academic/Plenum Publishers, New York, 1999.
80 M. Okubo, E. Hosono, J. Kim, M. Enomoto, N. Kojima, T. Kudo, H. S. Zhou and I. Honma, *J. Am. Chem. Soc.*, 2007, **129**, 7444–7452.
81 J. Wang, J. Polleux, J. Lim and B. Dunn, *J. Phys. Chem. C*, 2007, **111**, 14925–14931.
82 Y. Jiang and J. Liu, *Energy Environ. Mater.*, 2019, **2**, 30–37.
83 P. Srimuk, X. Su, J. Yoon, D. Aurbach and V. Presser, *Nat. Rev. Mater.*, 2020, **5**, 517–538.
84 Z. Liu, Z. Yue and H. Li, *Sep. Purif. Technol.*, 2020, **234**, 116090.
85 W. H. Shi, X. L. Gao, J. Mao, X. Qian, W. X. Liu, F. F. Wu, H. B. Li, Z. Y. Zeng, J. N. Shen and X. H. Cao, *Front. Chem.*, 2020, **8**, 9.
86 J. Lee, S. Kim and J. Yoon, *ACS Omega*, 2017, **2**, 1653–1659.
87 B. P. Jia and W. Zhang, *Nanoscale Res. Lett.*, 2016, **11**, 64.
88 Y. Liu, C. Y. Nie, X. J. Liu, X. T. Xu, Z. Sun and L. K. Pan, *RSC Adv.*, 2015, **5**, 15205–15225.
89 E. Avraham, Y. Bouhadana, A. Soffer and D. Aurbach, *J. Electrochem. Soc.*, 2009, **156**, 95–99.
90 M. Mossad and L. D. Zou, *Chem. Eng. J.*, 2013, **223**, 704–713.
91 H. L. Zhang, P. Liang, Y. H. Bian, Y. Jiang, X. L. Sun, C. Y. Zhang, X. Huang and F. Wei, *RSC Adv.*, 2016, **6**, 58907–58915.
92 Z. H. Huang, Z. Y. Yang, F. Y. Kang and M. Inagaki, *J. Mater. Chem. A*, 2017, **5**, 470–496.
93 P. I. Liu, L. C. Chung, C. H. Ho, H. Shao, T. M. Liang, M. C. Chang, C. C. M. Ma and R. Y. Horng, *Desalination*, 2016, **379**, 34–41.
94 Y. T. Qu, T. F. Baumann, J. G. Santiago and M. Stadermann, *Environ. Sci. Technol.*, 2015, **49**, 9699–9706.
95 M. Lenz, J. Zabel and M. Franzreb, *Front. Mater.*, 2020, **7**, 229.
96 H. B. Li, L. Zou, L. K. Pan and Z. Sun, *Sep. Purif. Technol.*, 2010, **75**, 8–14.
97 H. B. Li, L. D. Zou, L. K. Pan and Z. Sun, *Environ. Sci. Technol.*, 2010, **44**, 8692–8697.
98 T. N. Tuan, S. Chung, J. K. Lee and J. Lee, *Curr. Appl. Phys.*, 2015, **15**, 1397–1401.
99 H. Wang, D. S. Zhang, T. T. Yan, X. R. Wen, L. Y. Shi and J. P. Zhang, *J. Mater. Chem.*, 2012, **22**, 23745–23748.
100 K. Mohanapriya, G. Ghosh and N. Jha, *Electrochim. Acta*, 2016, **209**, 719–729.
101 A. Kalfa, T. R. Penki, I. Cohen, N. Shpigel, E. Avraham, D. Aurbach, D. W. Liang, Q. H. Wu, H. N. Wang and Y. Xiang, *Desalination*, 2020, **492**, 114599.
102 H. Lei, T. T. Yan, H. Wang, L. Y. Shi, J. P. Zhang and D. S. Zhang, *J. Mater. Chem. A*, 2015, **3**, 5934–5941.
103 Z. Li, B. Song, Z. K. Wu, Z. Y. Lin, Y. G. Yao, K. S. Moon and C. P. Wong, *Nano Energy*, 2015, **11**, 711–718.
104 M. Krishnamoorthy and N. Jha, *ACS Sustainable Chem. Eng.*, 2019, **7**, 8475–8489.
105 Y. Zhang, L. Chen, S. D. Mao, Z. Sun, Y. A. Song and R. Zhao, *J. Colloid Interface Sci.*, 2019, **536**, 252–260.

106 Y. X. Xu, K. X. Sheng, C. Li and G. Q. Shi, *ACS Nano*, 2010, **4**, 4324–4330.
107 Z. P. Chen, W. C. Ren, L. B. Gao, B. L. Liu, S. F. Pei and H. M. Cheng, *Nat. Mater.*, 2011, **10**, 424–428.
108 X. T. Xu, L. K. Pan, Y. Liu, T. Lu, Z. Sun and D. H. C. Chua, *Sci. Rep.*, 2015, **5**, 8458.
109 W. H. Shi, H. B. Li, X. H. Cao, Z. Y. Leong, J. Zhang, T. P. Chen, H. Zhang and H. Y. Yang, *Sci. Rep.*, 2016, **6**, 18966.
110 H. Wang, D. S. Zhang, T. T. Yan, X. R. Wen, J. P. Zhang, L. Y. Shi and Q. D. Zhong, *J. Mater. Chem. A*, 2013, **1**, 11778–11789.
111 X. R. Wen, D. S. Zhang, T. T. Yan, J. P. Zhang and L. Y. Shi, *J. Mater. Chem. A*, 2013, **1**, 12334–12344.
112 Z. Y. Yang, L. J. Jin, G. Q. Lu, Q. Q. Xiao, Y. X. Zhang, L. Jing, X. X. Zhang, Y. M. Yan and K. N. Sun, *Adv. Funct. Mater.*, 2014, **24**, 3917–3925.
113 Y. S. Zhu, G. J. Zhang, C. Xu and L. Z. Wang, *ACS Appl. Mater. Interfaces*, 2020, **12**, 29706–29716.
114 H. Y. Lian, S. Dutta, S. Tominaka, Y. A. Lee, S. Y. Huang, Y. Sakamoto, C. H. Hou, W. R. Liu, J. Henzie, Y. Yamauchi and K. C. W. Wu, *Small*, 2018, **14**, 1702054.
115 M. S. Zoromba, M. H. Abdel-Aziz, M. Bassyouni, S. Gutub, D. Demko and A. Abdelkader, *ACS Sustainable Chem. Eng.*, 2017, **5**, 4573–4581.
116 L. Chang and Y. H. Hu, *J. Phys. Chem. Solids*, 2019, **125**, 135–140.
117 L. Chang and Y. H. Hu, *J. Phys. Chem. Solids*, 2019, **134**, 64–68.
118 G. Q. Tan, R. Xu, Z. Y. Xing, Y. F. Yuan, J. Lu, J. G. Wen, C. Liu, L. Ma, C. Zhan, Q. Liu, T. P. Wu, Z. L. Jian, R. Shahbazian-Yassar, Y. Ren, D. J. Miller, L. A. Curtiss, X. L. Ji and K. Amine, *Nat. Energy*, 2017, **2**, 17090.
119 L. Sun, J. Z. Liu, Z. H. Liu, T. Wang, H. X. Wang and Y. Li, *RSC Adv.*, 2018, **8**, 19964–19970.
120 Z. Y. Xing, B. Wang, W. Y. Gao, C. Q. Pan, J. K. Halsted, E. S. Chong, J. Lu, X. F. Wang, W. Luo, C. H. Chang, Y. H. Wen, S. Q. Ma, K. Amine and X. L. Ji, *Nano Energy*, 2015, **11**, 600–610.
121 B. Han, G. Cheng, Y. K. Wang and X. K. Wang, *Chem. Eng. J.*, 2019, **360**, 364–384.
122 D. C. Han, C. M. Zhang, J. Guan, L. H. Gai, R. Y. Yue, L. N. Liu, M. Z. Afzal, C. Song, S. G. Wang and X. F. Sun, *Electrochim. Acta*, 2020, **336**, 135639.
123 B. P. Jia and L. D. Zou, *Chem. Phys. Lett.*, 2012, **548**, 23–28.
124 B. P. Jia and L. D. Zou, *Carbon*, 2012, **50**, 2315–2321.
125 T. Bala, B. L. V. Prasad, M. Sastry, M. U. Kahaly and U. V. Waghmare, *J. Phys. Chem. A*, 2007, **111**, 6183–6190.
126 X. T. Xu, L. K. Pan, Y. Liu, T. Lu and Z. Sun, *J. Colloid Interface Sci.*, 2015, **445**, 143–150.
127 M. Qian, M. N. Duan and Z. D. Gong, *Int. J. Energy Res.*, 2019, **43**, 7583–7593.
128 Z. U. Khan, T. T. Yan, J. L. Han, L. Y. Shi and D. S. Zhang, *Environ. Sci.: Nano*, 2019, **6**, 3442–3453.
129 M. Wang, X. T. Xu, J. Tang, S. J. Hou, M. S. A. Hossain, L. K. Pan and Y. Yamauchi, *Chem. Commun.*, 2017, **53**, 10784–10787.
130 Y. Belaustegui, S. Zorita, F. Fernandez-Carretero, A. Garcia-Luis, F. Panto, S. Stelitano, P. Frontera, P. Antonucci and S. Santangelo, *Desalination*, 2018, **428**, 40–49.
131 X. T. Xu, Z. Sun, D. H. C. Chua and L. K. Pan, *Sci. Rep.*, 2015, **5**, 11225.
132 H. B. Li, F. Zaviska, S. Liang, J. Li, L. J. He and H. Y. Yang, *J. Mater. Chem. A*, 2014, **2**, 3484–3491.
133 X. K. Huang, X. R. Guo, Q. Q. Dong, L. J. Liu, R. Tallon and J. H. Chen, *Environ. Sci.: Nano*, 2019, **6**, 3225–3231.
134 L. Chang and Y. H. Hu, *J. Colloid Interface Sci.*, 2019, **538**, 420–425.
135 X. M. Zhang, K. J. Xie, J. J. Gao, S. P. Zhang, S. Wang, C. Ma and H. Song, *Desalination*, 2018, **445**, 149–158.
136 S. Hu, K. J. Xie, X. M. Zhang, S. P. Zhang, J. J. Gao, H. O. Song and D. Z. Chen, *Chem. Eng. J.*, 2020, **384**, 123317.
137 H. L. Zhang, P. Liang, Y. H. Bian, X. L. Sun, J. J. Ma, Y. Jiang and X. Huang, *Sep. Purif. Technol.*, 2018, **194**, 451–456.
138 O. ul Haq, D. S. Choi, J. H. Choi and Y. S. Lee, *J. Ind. Eng. Chem.*, 2020, **83**, 136–144.
139 A. G. El-Deen, R. M. Boom, H. Y. Kim, H. W. Duan, M. B. Chan-Park and J. H. Choi, *ACS Appl. Mater. Interfaces*, 2016, **8**, 25313–25325.
140 P. Y. Liu, H. Wang, T. T. Yan, J. P. Zhang, L. Y. Shi and D. S. Zhang, *J. Mater. Chem. A*, 2016, **4**, 5303–5313.
141 P. Y. Liu, T. T. Yan, J. P. Zhang, L. Y. Shi and D. S. Zhang, *J. Mater. Chem. A*, 2017, **5**, 14748–14757.
142 Y. Liao, M. Wang and D. J. Chen, *Appl. Surf. Sci.*, 2019, **484**, 83–96.
143 G. Zhu, W. Q. Wang, X. L. Li, J. Zhu, H. Y. Wang and L. Zhang, *RSC Adv.*, 2016, **6**, 5817–5823.
144 H. O. Song, Y. F. Wu, S. P. Zhang, W. T. Li, B. J. Wang, C. M. Wang, J. J. Gao and A. M. Li, *Electrochim. Acta*, 2016, **205**, 161–169.
145 H. B. Li, L. K. Pan, C. Y. Nie, Y. Liu and Z. Sun, *J. Mater. Chem.*, 2012, **22**, 15556–15561.
146 H. Wang, L. Y. Shi, T. T. Yan, J. P. Zhang, Q. D. Zhong and D. S. Zhang, *J. Mater. Chem. A*, 2014, **2**, 4739–4750.
147 H. B. Li, S. Liang, J. Li and L. J. He, *J. Mater. Chem. A*, 2013, **1**, 6335–6341.
148 Y. T. Lai, W. T. Liu, L. C. Chung, P. I. Liu, M. C. Chang, R. Y. Horng, L. J. Chen, C. Y. Lee and N. H. Tai, *Adv. Mater. Technol.*, 2019, **4**, 1900213.
149 K. Mohanapriya and N. Jha, *Electrochim. Acta*, 2019, **324**, 134870.
150 S. Vafakhah, G. J. Sim, M. Saeedikhani, X. X. Li, P. V. Y. Alvarado and H. Y. Yang, *Nanoscale Adv.*, 2019, **1**, 4804–4811.
151 Z. U. Khan, T. T. Yan, L. Y. Shi and D. S. Zhang, *Environ. Sci.: Nano*, 2018, **5**, 980–991.
152 L. Liu, L. H. Liao, Q. H. Meng and B. Cao, *Carbon*, 2015, **90**, 75–84.
153 O. Noonan, Y. Liu, X. D. Huang and C. Z. Yu, *J. Mater. Chem. A*, 2018, **6**, 14272–14280.
154 X. T. Xu, Y. Liu, T. Lu, Z. Sun, D. H. C. Chua and L. K. Pan, *J. Mater. Chem. A*, 2015, **3**, 13418–13425.
155 D. S. Zhang, T. T. Yan, L. Y. Shi, Z. Peng, X. R. Wen and J. P. Zhang, *J. Mater. Chem.*, 2012, **22**, 14696–14704.

156 Y. Wimalasiri and L. D. Zou, *Carbon*, 2013, **59**, 464–471.
157 J. L. Cao, Y. Wang, C. Y. Chen, F. Yu and J. Ma, *J. Colloid Interface Sci.*, 2018, **518**, 69–75.
158 G. Wang, Q. Dong, T. T. Wu, F. Zhan, M. Zhou and J. S. Qiu, *Carbon*, 2016, **103**, 311–317.
159 Q. Dong, G. Wang, B. Q. Qian, C. Hu, Y. W. Wang and J. S. Qiu, *Electrochim. Acta*, 2014, **137**, 388–394.
160 Y. Bai, Z. H. Huang, X. L. Yu and F. Y. Kang, *Colloids Surf., A*, 2014, **444**, 153–158.
161 Y. Liu, X. T. Xu, T. Lu, Z. Sun, D. H. C. Chua and L. K. Pan, *RSC Adv.*, 2015, **5**, 34117–34124.
162 C. Zhang, X. D. Wang, H. Q. Wang, X. L. Wu and J. Shen, *Processes*, 2019, **7**, 29.
163 Y. Liu, C. Y. Nie, L. K. Pan, X. T. Xu, Z. Sun and D. H. C. Chua, *Inorg. Chem. Front.*, 2014, **1**, 249–255.
164 X. Yu, S. Yun, J. S. Yeon, P. Bhattacharya, L. B. Wang, S. W. Lee, X. L. Hu and H. S. Park, *Adv. Energy Mater.*, 2018, **8**, 1702930.
165 Z. Wang, B. J. Dou, L. Zheng, G. N. Zhang, Z. H. Liu and Z. P. Hao, *Desalination*, 2012, **299**, 96–102.
166 Z. Wang, L. Yue, Z. T. Liu, Z. H. Liu and Z. P. Hao, *J. Mater. Chem.*, 2012, **22**, 14101–14107.
167 G. M. Luo, Y. Z. Wang, L. X. Gao, D. Q. Zhang and T. Lin, *Electrochim. Acta*, 2018, **260**, 656–663.
168 C. Yan, Y. W. Kanaththage, R. Short, C. T. Gibson and L. D. Zou, *Desalination*, 2014, **344**, 274–279.
169 H. Liu, J. Zhang, X. X. Xu and Q. Wang, *Chem.–Eur. J.*, 2020, **26**, 4403–4409.
170 K. Xu, Y. H. Liu, Z. H. An, G. R. Xu, A. J. Gadgil and G. L. Ruan, *Desalination*, 2020, **486**, 114407.
171 J. Q. Xue, Q. X. Sun, Y. J. Zhang, W. B. Mao, F. G. Li and C. X. Yin, *ACS Omega*, 2020, **5**, 10995–11004.
172 H. B. Yu, M. Che, B. Zhao, Y. Lu, S. Y. Zhu, X. H. Wang, W. C. Qin and M. X. Huo, *Synth. Met.*, 2020, **262**, 116332.
173 Y. M. Zhang, L. D. Zou, Y. Wimalasiri, J. Y. Lee and Y. Chun, *Electrochim. Acta*, 2015, **182**, 383–390.
174 A. Alabi, L. Cseri, A. Al Hajaj, G. Szekely, P. Budd and L. D. Zou, *J. Membr. Sci.*, 2020, **594**, 117457.
175 S. Chaudhury, A. K. Thakur, R. S. Gojman, C. J. Arnusch and O. Nir, *J. Phys. Chem. Lett.*, 2020, **11**, 1397–1403.
176 A. G. El-Deen, N. A. M. Barakat and H. Y. Kim, *Desalination*, 2014, **344**, 289–298.
177 X. Y. Gu, Y. Yang, Y. Hu, M. Hu and C. Y. Wang, *ACS Sustainable Chem. Eng.*, 2015, **3**, 1056–1065.
178 S. K. Sami, J. Y. Seo, S. E. Hyeon, M. S. A. Shershah, P. J. Yoo and C. H. Chung, *RSC Adv.*, 2018, **8**, 4182–4190.
179 H. B. Li, Z. Y. Leong, W. H. Shi, J. Zhang, T. P. Chen and H. Y. Yang, *RSC Adv.*, 2016, **6**, 11967–11972.
180 A. G. El-Deen, J. H. Choi, C. S. Kim, K. A. Khalil, A. A. Almajid and N. A. M. Barakat, *Desalination*, 2015, **361**, 53–64.
181 A. Yousef, A. M. Al-Enizi, I. M. A. Mohamed, M. M. El-Halwany, M. Ubaidullah and R. M. Brooks, *Ceram. Int.*, 2020, **46**, 15034–15043.
182 A. S. Yasin, H. O. Mohamed, I. M. A. Mohamed, H. M. Mousa and N. A. M. Barakat, *Sep. Purif. Technol.*, 2016, **171**, 34–43.
183 N. Arora, F. Banat, G. Bharath and E. Alhseinat, *J. Phys. D: Appl. Phys.*, 2019, **52**, 455304.
184 M. A. Jaoude, E. Alhseinat, K. Polychronopoulou, G. Bharath, I. F. F. Darawsheh, S. Anwer, M. A. Baker, S. J. Hinder and F. Banat, *Electrochim. Acta*, 2020, **330**, 135202.
185 X. Y. Gu, Y. Yang, Y. Hu, M. Hu, J. Huang and C. Y. Wang, *J. Mater. Chem. A*, 2015, **3**, 5866–5874.
186 A. G. El-Deen, N. A. M. Barakat, K. A. Khalil, M. Motlak and H. Y. Kim, *Ceram. Int.*, 2014, **40**, 14627–14634.
187 H. M. Moustafa, M. Obaid, M. M. Nassar, M. A. Abdelkareem and M. S. Mahmoud, *Sep. Purif. Technol.*, 2020, **235**, 116178.
188 J. P. L. Lazarte, L. Bautista-Patacsil, R. C. P. Eusebio, A. H. Orbecido and R. A. Doong, *Nanomaterials*, 2019, **9**, 1319.
189 A. B. Ganganboina and R. A. Doong, *Environ. Sci.: Nano*, 2020, **7**, 228–237.
190 H. J. Yin, S. L. Zhao, J. W. Wan, H. J. Tang, L. Chang, L. C. He, H. J. Zhao, Y. Gao and Z. Y. Tang, *Adv. Mater.*, 2013, **25**, 6270–6276.
191 G. Bharath, E. Alhseinat, N. Ponpandian, M. A. Khan, M. R. Siddiqui, F. Ahmed and E. H. Alsharaeh, *Sep. Purif. Technol.*, 2017, **188**, 206–218.
192 G. Bharath, N. Arora, A. Hai, F. Banat, D. Savariraj, H. Taher and R. V. Mangalaraja, *Electrochim. Acta*, 2020, **337**, 135668.
193 M. Dai, M. Zhang, L. Xia, Y. M. Li, Y. Y. Liu and S. X. Song, *ACS Sustainable Chem. Eng.*, 2017, **5**, 6532–6538.
194 H. Younes, F. Ravaux, N. El Hadri and L. D. Zou, *Electrochim. Acta*, 2019, **306**, 1–8.
195 H. Younes and L. D. Zou, *Environ. Sci.: Water Res. Technol.*, 2020, **6**, 392–403.
196 W. Xi and H. B. Li, *Environ. Sci.: Nano*, 2020, **7**, 764–772.
197 Q. D. Ren, G. Wang, T. T. Wu, X. He, J. R. Wang, J. Yang, C. Yu and J. S. Qiu, *Ind. Eng. Chem. Res.*, 2018, **57**, 6417–6425.
198 D. Z. Li, S. Y. Wang, G. Wang, C. X. Li, X. P. Che, S. F. Wang, Y. Q. Zhang and J. S. Qiu, *ACS Appl. Mater. Interfaces*, 2019, **11**, 31200–31209.
199 F. Xing, T. Li, J. Y. Li, H. R. Zhu, N. Wang and X. Cao, *Nano Energy*, 2017, **31**, 590–595.
200 W. J. Peng, W. Wang, G. H. Han, Y. K. Huang and Y. S. Zhang, *Desalination*, 2020, **473**, 114191.
201 J. L. Han, T. T. Yan, J. J. Shen, L. Y. Shi, J. P. Zhang and D. S. Zhang, *Environ. Sci. Technol.*, 2019, **53**, 12668–12676.
202 L. J. Gao, Q. Dong, S. L. Bai, S. C. Liang, C. Hu and J. S. Qiu, *ACS Sustainable Chem. Eng.*, 2020, **8**, 9690–9697.
203 N. T. Trinh, S. Chung, J. K. Lee and J. Lee, *J. Energy Chem.*, 2016, **25**, 354–360.
204 G. Divyapriya, K. K. Vijayakumar and I. Nambi, *Desalination*, 2019, **451**, 102–110.
205 F. Zhou, T. Gao, M. Luo and H. B. Li, *Chem. Eng. J.*, 2018, **343**, 8–15.
206 D. Sriramulu and H. Y. Yang, *Nanoscale*, 2019, **11**, 5896–5908.
207 C. X. Li, S. Y. Wang, G. Wang, S. F. Wang, X. P. Che, D. Z. Li and J. S. Qiu, *Environ. Sci.: Water Res. Technol.*, 2020, **6**, 303–311.

208 M. R. Vengatesan, E. Alhseinat, A. F. Arangadi, S. Anwer, Y. Y. Kannangara, J. K. Song and F. Banat, *Sep. Purif. Technol.*, 2019, **229**, 115799.
209 X. Y. Zhao, M. H. Feng, Y. X. Jiao, Y. B. Zhang, Y. F. Wang and Z. L. Sha, *Desalination*, 2020, **481**, 114360.
210 B. Q. Wang, Y. Han, X. Wang, N. Bahlawane, H. G. Pan, M. Yan and Y. Z. Jiang, *Iscience*, 2018, **3**, 110–133.
211 S. Vafakhah, L. Guo, D. Sriramulu, S. Z. Huang, M. Saeedikhani and H. Y. Yang, *ACS Appl. Mater. Interfaces*, 2019, **11**, 5989–5998.
212 Z. B. Ding, X. T. Xu, Y. Q. Li, K. Wang, T. Lu and L. K. Pan, *Desalination*, 2019, **468**, 114078.
213 J. Ma, L. Wang, F. Yu and X. H. Dai, *Chem. Eng. J.*, 2019, **370**, 938–943.
214 L. Guo, Y. X. Huang, M. Ding, Z. Y. Leong, S. Vafakhah and H. Y. Yang, *J. Mater. Chem. A*, 2018, **6**, 8901–8908.
215 Y. X. Huang, F. M. Chen, L. Guo and H. Y. Yang, *J. Mater. Chem. A*, 2017, **5**, 18157–18165.
216 C. L. Han, Q. H. Meng, B. Cao and G. Y. Tian, *ACS Omega*, 2019, **4**, 11455–11463.
217 S. J. Liang, C. L. Han, Q. H. Meng and G. Y. Tian, *J. Mater. Sci.*, 2020, **55**, 6017–6029.
218 W. Y. Zhao, M. Ding, L. Guo and H. Y. Yang, *Small*, 2019, **15**, 1805505.
219 Y. J. Fang, J. X. Zhang, L. F. Xiao, X. P. Ai, Y. L. Cao and H. X. Yang, *Adv. Sci.*, 2017, **4**, 1600392.
220 X. T. Xu, Y. Liu, M. Wang, X. X. Yang, C. Zhu, T. Lu, R. Zhao and L. K. Pan, *Electrochim. Acta*, 2016, **188**, 406–413.
221 X. D. Wu, K. W. Li, S. J. H. Ying, L. Liu, M. Wang and Y. Liao, *J. Radioanal. Nucl. Chem.*, 2019, **321**, 977–984.
222 A. Amiri, G. Ahmadi, M. Shanbedi, M. Savari, S. N. Kazi and B. T. Chew, *Sci. Rep.*, 2015, **5**, 17503.
223 A. M. Abdelkader and D. J. Fray, *Nanoscale*, 2017, **9**, 14548–14557.
224 L. J. Liu, X. R. Guo, R. Tallon, X. K. Huang and J. H. Chen, *Chem. Commun.*, 2017, **53**, 881–884.
225 Q. H. Ji, C. Z. Hu, H. J. Liu and J. H. Qu, *Chem. Eng. J.*, 2018, **350**, 608–615.
226 S. S. Wang, J. W. Feng, Q. H. Meng, B. Cao and G. Y. Tian, *J. Solid State Electrochem.*, 2019, **23**, 2377–2390.
227 T. T. Yan, J. Liu, H. Lei, L. Y. Shi, Z. X. An, H. S. Park and D. S. Zhang, *Environ. Sci.: Nano*, 2018, **5**, 2722–2730.
228 A. T. U. Nugrahenny, J. Kim, S. K. Kim, D. H. Peck, S. H. Yoon and D. H. Jung, *Carbon Lett.*, 2014, **15**, 38–44.
229 P. H. Wang, G. Q. Lu, H. Yan, W. Ni, M. Xu, Y. F. Xue and Y. M. Yan, *RSC Adv.*, 2016, **6**, 70532–70536.
230 D. S. Zhang, X. R. Wen, L. Y. Shi, T. T. Yan and J. P. Zhang, *Nanoscale*, 2012, **4**, 5440–5446.
231 H. T. Zhang, K. Wang, X. Zhang, H. Lin, X. Z. Sun, C. Li and Y. W. Ma, *J. Mater. Chem. A*, 2015, **3**, 11277–11286.
232 F. Yue, Q. Zhang, L. J. Xu, Y. Q. Zheng, C. X. Yao, J. N. Jia, W. N. Leng and S. F. Hou, *ACS Appl. Nano Mater.*, 2019, **2**, 6258–6267.
233 X. T. Xu, Y. Liu, M. Wang, C. Zhu, T. Lu, R. Zhao and L. K. Pan, *Electrochim. Acta*, 2016, **193**, 88–95.
234 X. Y. Gu, Y. Yang, Y. Hu, M. Hu, J. Huang and C. Y. Wang, *RSC Adv.*, 2014, **4**, 63189–63199.
235 M. J. Mi, X. J. Liu, W. Q. Kong, Y. J. Ge, W. Q. Dang and J. W. Hu, *Desalination*, 2019, **464**, 18–24.
236 X. Y. Gu, M. Hu, Z. S. Du, J. Huang and C. Y. Wang, *Electrochim. Acta*, 2015, **182**, 183–191.